The Journal of Chemical Physics

RESEARCH ARTICLE | DECEMBER 04 2025

Protonated phosphorus mononitride: Spectroscopic parameters and formation routes relevant for astrochemistry

Special Collection: 2025 JCP Emerging Investigators Special Collection

D. Comte ; M. Melosso ; S. Alessandrini ; L. Bizzocchi ; V. M. Rivilla ; I. Jiménez-Serra ;
C. Puzzarini

J. Chem. Phys. 163, 214306 (2025)
https://doi.org/10.1063/5.0304579

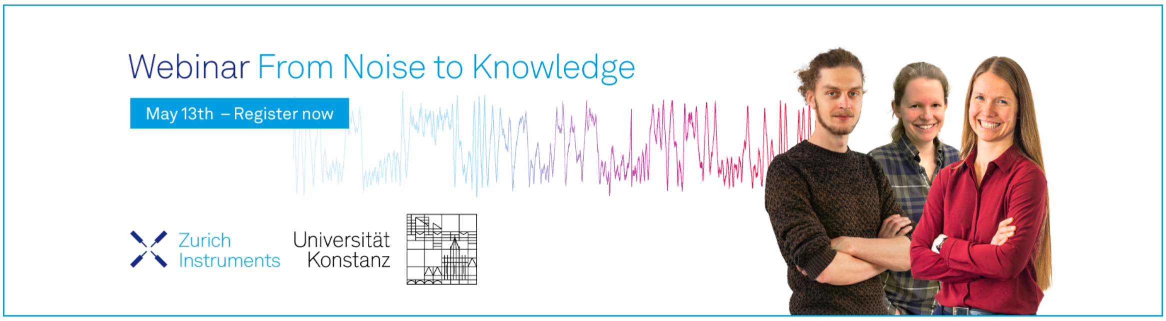

AIP Publishing

The Journal of Chemical Physics ARTICLE pubs.aip.org/aip/jcp

Protonated phosphorus mononitride: Spectroscopic parameters and formation routes relevant for astrochemistry

Cite as: J. Chem. Phys. 163, 214306 (2025); doi: 10.1063/5.0304579
Submitted: 29 September 2025 • Accepted: 10 November 2025 •
Published Online: 4 December 2025

D. Comte,[1,a)] M. Melosso,[2,b)] S. Alessandrini,[2] L. Bizzocchi,[2] V. M. Rivilla,[3] I. Jiménez-Serra,[3] and C. Puzzarini[2]

AFFILIATIONS

[1] Scuola Superiore Meridionale, Largo San Marcellino 10, 80138 Naples, Italy
[2] Dipartimento di Chimica "Giacomo Ciamician," Università di Bologna, Via P. Gobetti 85, 40129 Bologna, Italy
[3] Centro de Astrobiología (CSIC-INTA), Ctra. de Ajalvir Km. 4, Torrejón de Ardoz, 28850 Madrid, Spain

Note: This paper is a part of the 2025 JCP Emerging Investigators Special Collection.
[a)] **Author to whom correspondence should be addressed:** d.comte@ssmeridionale.it
[b)] **Electronic mail:** mattia.melosso2@unibo.it

ABSTRACT

Phosphorus-bearing molecules are of growing interest in astrochemistry because of the essential role of phosphorus in biochemistry. Understanding their interstellar chemistry requires both accurate spectroscopic data and insights into their formation mechanisms. In this work, for a new possible phosphorus-bearing species, protonated phosphorus mononitride, PNH^+, we present a high-level theoretical study, which combines an accurate spectroscopic characterization with a thermochemical and kinetic investigation of its formation pathways. The key spectroscopic parameters, computed by exploiting composite schemes rooted in coupled-cluster theory, refer to both rotational and vibrational spectroscopy, thus including rotational and centrifugal distortion constants, hyperfine parameters, as well as vibrational frequencies and infrared intensities. To assess their accuracy for PNH^+, a comparison with those of the isovalent N_2H^+, HCO^+, and HCS^+ ions, whose experimental characterization is available, has been made. In parallel, we investigated three gas-phase formation reactions relevant to interstellar conditions: the protonation of PN by H_3^+ and the ion–neutral PH + NH^+ and PH^+ + NH reactions. For each process, the reactive potential energy surface is sampled using density functional theory, and reaction rate coefficients are derived from long-range capture theory and master equation analysis. These rates were then incorporated into a dedicated astrochemical model to discuss the expected abundance of PNH^+ in the interstellar medium. The results show that, under interstellar conditions, multiple exothermic pathways can lead to PNH^+, thus reinforcing its potential role in interstellar phosphorus chemistry.

I. INTRODUCTION

Phosphorus (hereafter P) plays a fundamental role in the origin and maintenance of life, as a key component of nucleic acids and energy carriers such as adenosine triphosphate (ATP).[1] This biological relevance has made P-containing compounds important targets in both astronomical observations and astrochemical modeling. However, the identification of P-bearing species remains limited in the interstellar medium (ISM), thus highlighting the challenge of spectroscopic characterization at the basis of subsequent detection, as well as their low abundance in the gas phase. Nevertheless, as shown by Fontani,[2] several small P-containing molecules have been identified in various astrophysical environments, including star-forming regions and circumstellar envelopes. Among them, phosphorus mononitride (PN)[3,4]—the first P-bearing species detected, in 1987—is the most widely observed,[5–7] along with other neutral diatomics such as phosphorus monoxide (PO)[8] and carbon monophosphide (CP).[9] Additional detections include phosphine

(PH_3),[10,11] phosphaethyne (HCP),[12] cyanoethyl phosphine (CCP),[13] and the ionized phosphorus monoxide (PO^+),[14,15] as well as a tentative detection of silicon monophosphide (SiP), claimed by Koelemay *et al.*[16]

Understanding the mechanisms behind the emergence of P-based chemical complexity remains a major challenge for astrochemical models. As in the chemistry of carbon (C), oxygen (O), and nitrogen (N), this complexity likely arises from a combination of gas-phase and grain-surface processes.[17] Among the gas-phase mechanisms, ion–neutral reactions are particularly important due to their typically high capture rate coefficients and their ability to proceed without activation barriers—making them especially relevant under the low-temperature and low-density conditions of the ISM. Within this group, protonation reactions play a key role. The central molecule is H_3^+, which acts as an effective proton donor because the proton affinity (PA) of H_2 is relatively low (4.4 eV[18]), thus making proton transfer to most atoms and molecules particularly efficient and enabling the widespread formation of protonated species. Numerous such species have been detected in the ISM, ranging from protonated diatomics N_2H^+,[19] HCO^+,[19] and HCS^+,[20] to more complex ions such as $HCNH^+$,[21] $HCCCNH^+$,[21] and H_2COH^+.[22] In turn, these protonated ions can drive the production of more complex neutral molecules through subsequent ion–neutral reactions and dissociative recombination. As an example, a potential formation pathway of protonated dimethyl ether in the ISM has been suggested to be the reaction between protonated methanol and neutral methanol.[23,24] Moreover, protonated molecules can promote the formation of stable molecular clusters, increasing interaction times and introducing new relaxation pathways, such as evaporation, that may protect molecular systems from external radiations or collisions.[25,26]

Radioastronomy, through the observation of radiation emitted from astrophysical objects in the cm- to submm-wave regions (which corresponds to rotational transitions), remains the most powerful tool for detecting and identifying molecules in the ISM. This successful result arises from the high sensitivity of rotational spectra to molecular structure and mass composition, which thus enables the confident identification of new species and the derivation of the chemical inventory in diverse astronomical environments. Accurate spectroscopic parameters or, better, the line catalogs they allow to set up, are thus essential for guiding observations.[27] In parallel, astrochemical modeling plays a central role in linking observed molecular abundances to the underlying chemistry. Astrochemical models strongly rely on the rates of chemical reactions involved in the formation and destruction of molecules, which, in the gas phase, are dominated by radical–neutral and ion–neutral reactions at the low temperatures of the ISM. Therefore, theoretical determination of such rates, whenever experimental data are unavailable—which is often the case—is crucial for evaluating the viability of proposed mechanisms and improving the predictive power of astrochemical networks.

In the case of P chemistry, the role of protonated species must be carefully examined to correctly interpret both current and future astronomical observations and to understand the chemical complexity in space. The diatomic molecule PN is considered one of the primary gas-phase reservoirs of P in the ISM, and its protonated counterpart could represent an entry point toward more complex P-bearing molecules. The aim of this study is to provide a detailed spectroscopic characterization of the lowest-energy structure of protonated phosphorus mononitride, PNH^+, along with a theoretical investigation of three astrochemically relevant formation reactions. The spectroscopic analysis is supported by a validation of the computational methodology based on the comparison of experiment and theory for the isovalent species N_2H^+, HCO^+, and HCS^+. On the reactivity side, potential energy surfaces (PESs) and temperature-dependent capture and reaction rate coefficients are derived to assess the viability of each formation pathway under interstellar conditions. Finally, these results are incorporated into an astrochemical model to discuss the expected abundances of PNH^+ within interstellar environments.

II. COMPUTATIONAL DETAILS

Neutral molecules can be subjected to structural and electronic rearrangements upon protonation. For this reason, we first investigated the stability of linear and bent structures of PNH^+ and HPN^+, considering both singlet and triplet electronic states. This preliminary study was carried out using density functional theory (DFT), choosing the double-hybrid rev-DSD-PBEP86 functional[28] and incorporating the D3BJ empirical dispersion correction.[29,30] This functional was combined with the jun-cc-pVTZ basis set, for N and H, and the jun-cc-pV(T+d)Z basis set,[31,32] for P. This level of theory is hereafter referred to as revDSD/jun(T+d)Z. The ground state was found to be a linear singlet, which will be the only configuration considered in the following spectroscopic study and the main focus of the reactivity investigation. For clarity, the astrochemical modeling section of this work is presented in a dedicated section, where the methodology and results are discussed together.

A. Rotational and vibrational spectroscopy

In the field of rotational spectroscopy, the parameters considered in this work include the rotational and centrifugal distortion (quartic and sextic) constants together with the hyperfine parameters (namely, the nuclear quadrupole coupling, nuclear spin–rotation interaction, and dipolar spin–spin coupling constants) to determine the spectral line positions, and the electric dipole moment to derive their intensity. Moving to vibrational spectroscopy, the fundamental (anharmonic) vibrational frequencies and their infrared (IR) intensity have been computed.

Focusing on rotational spectroscopy, the most influential parameter is the vibrational ground-state rotational constant, B_0, which is a unique parameter because of the linearity of the considered ions. According to vibrational perturbation theory to second order (VPT2),[33] the ground-state rotational constant consists of two terms, the equilibrium contribution B_e and a vibrational correction ΔB_{vib}. To these two terms, an electronic contribution ΔB_{el} can also be added. Therefore, B_0 is defined as

$$B_0 = B_e + \Delta B_{vib} + \Delta B_{el} = B_e - \sum_k \frac{d_k}{2}\alpha_k + \frac{m_e}{m_p} g B_e, \qquad (1)$$

where B_e is straightforwardly derived from the molecule's equilibrium geometry and isotopic composition. The second term, ΔB_{vib}, is determined from the vibration–rotation interaction constants, α_k, the sum running over all vibration modes, with d_k denoting their degeneracy. In the final term of Eq. (1), m_e and m_p are the electron and proton masses, respectively, and g is the component of the rotational g-tensor.[34,35] As pointed out in Ref. 34, these corrections are crucial for reaching the accuracy required for a quantitative comparison with experimental data. Although typically smaller than the vibrational correction, the electronic contribution can significantly improve the overall accuracy of the predictions.[36]

In this work, the equilibrium geometry (bond distances), the electric dipole moment, the nuclear quadrupole coupling constants (NQCCs), the harmonic frequencies and the associated IR intensities, and the quartic centrifugal distortion constant were predicted using a quantum-chemical composite scheme that combines several coupled-cluster (CC) calculations relying on the additivity approximation. The scheme can be summarized as follows:

$$\begin{aligned}\rho_e = \rho^{\infty}(\text{HF-SCF}) + \Delta\rho^{\infty}(\text{CCSD(T)}) \\ + \Delta\rho(\text{CV}) + \Delta\rho(\text{fT}) + \Delta\rho(\text{fQ}) \;,\end{aligned} \tag{2}$$

where ρ_e defines a generic parameter from the list reported above. The first two terms represent the extrapolation to the complete basis set (CBS) limit and aim to minimize as much as possible the basis-set truncation error. The Hartree–Fock self-consistent (HF-SCF) terms were computed using correlation-consistent polarized basis sets cc-pVnZ,[31,37–39] with n = Q, 5, 6, and extrapolated to the CBS limit employing the three-point formula by Feller.[40] The correlation energy correction, evaluated using the CCSD(T) method[41] (i.e., coupled-cluster singles and doubles augmented by a perturbative treatment of triples), was computed in conjunction with the cc-pV5Z and cc-pV6Z basis sets, within the frozen-core (fc) approximation, and extrapolated by means of the n^{-3} formula introduced by Helgaker *et al.*[42] The third term, $\Delta\rho(\text{CV})$, accounts for core–valence correlation effects and was computed as the difference between all-electron (ae) and fc-CCSD(T) calculations in the cc-pCVQZ basis set[43] for molecules without third-row atoms. For PNH^+ and HCS^+, the cc-pwCVQZ basis set[44] was used instead. According to Ref. 44, the 1s electrons of P and sulfur (S) were excluded from ae computations. The fourth contribution, $\Delta\rho(\text{fT})$, incorporates the correction due to the full treatment of triple excitations and was calculated as the difference between fc-CCSDT[45,46] (coupled-cluster singles, doubles, and triples) and fc-CCSD(T) computations in the cc-pVTZ basis set. Finally, the fifth term, $\Delta\rho(\text{fQ})$, captures the effects of the full treatment of quadruple excitations; this was computed as the difference between fc-CCSDTQ[47,48] (coupled-cluster singles, doubles, triples, and quadruples) and fc-CCSDT calculations in conjunction with the cc-pVDZ basis set. The highest level of theory, which incorporates all the five contributions, is hereafter referred to as "CBS+CV+fT+fQ" or simply *full*.

The equilibrium geometry obtained through the composite scheme [Eq. (2)] was used to derive the equilibrium rotational constant B_e value. First-order properties, such as the electric dipole moment and electric field gradient (EFG) tensor, were determined on top of the best (*full*) geometry, also applying the "CBS+CV+fT+fQ" composite scheme. From the EFG tensor, the nuclear quadrupole coupling constants (NQCCs) are obtained by multiplying each component by the nuclear quadrupole moment of the corresponding nucleus.[34] We note that in the case of NQCCs, a non-monotonic behavior has been observed in the extension of HF calculations toward the CBS limit; thus, the CBS term for NQCCs has been derived only with the n^{-3} formula of Helgaker *et al.*[42] applied to the EFG components obtained with the CCSD(T) method in the cc-pV5Z and cc-pV6Z basis sets. The equilibrium rotational constant, electric dipole moment, and NQCCs were then corrected for vibrational effects. These corrections were derived from VPT2 calculations applied to an anharmonic force field evaluated at the ae-CCSD(T)/cc-pCVQZ level of theory for N_2H^+ and HCO^+ and at the ae-CCSD(T)/cc-pwCVQZ level for HCS^+ and PNH^+. In passing, we note that nuclear quadrupole coupling only arises whenever the molecule contains quadrupolar nuclei, that is, with nuclear spin $I > 1/2$. In this study, it applies to PNH^+ and N_2H^+ because of N $(I = 1)$. For the latter, a value of 20.44 mbarn[49,50] for the quadrupole moment was used to derive the NQCCs. Furthermore, a harmonic force field calculation was performed at each geometry optimization step within the composite scheme. This allowed for the determination of quartic centrifugal distortion constants and harmonic frequencies (ω_i), along with their IR intensities, at the *full* level of theory. Anharmonic force field calculations exploiting the VPT2 treatment yielded the anharmonic contributions to the fundamental vibrational frequencies (ν_i), and their IR intensities, and also provided the sextic centrifugal distortion constants.

On top of the *full* equilibrium geometry, electronic corrections to the rotational constants, as described in Eq. (1), were computed at the fc-CCSD(T)/aug-cc-pVTZ level. Using the same equilibrium geometry, we also evaluate the nuclear spin–rotation interaction tensor (SRT) and the dipolar spin–spin coupling tensor (DCT). While for details on the theoretical background of the SRT and DCT, the reader is referred to Refs. 51–53, a brief overview is presented here. The SRT has non-zero components whenever the nuclear spin $I \geq 1/2$. It consists of an electronic component, defined as the second derivative of the electronic energy with respect to both the rotational angular momentum and nuclear spin,[54,55] and a nuclear component, which is completely determined by the molecular geometry. The equilibrium SRT was computed at the ae-CCSD(T)/aug-cc-pCVQZ level for N_2H^+ and HCO^+ and at the ae-CCSD(T)/aug-cc-pwCVQZ level for HCS^+ and PNH^+. Owing to the linearity of the studied molecules, all investigated in their vibrational ground-state, a unique value is sufficient to characterize the SRT, $\boldsymbol{C}(L)$, of the atom L, and the following relations hold:[52]

$$C(L) = C_{xx}(L) = C_{yy}(L), \tag{3}$$

$$C_{zz}(L) = 0. \tag{4}$$

Here, $C(L)$ denotes the spin–rotation interaction constant associated with atom L. The DCT arises from a magnetic interaction between two nuclei, each possessing a non-zero nuclear spin. Similarly to the SRT, for the DCT, $\boldsymbol{D}^{LM}$ (where L and M refer to the interacting nuclei), of linear molecules, all off-diagonal components are zero, and only one element per nuclear pair is sufficient,[53]

$$D_{LM} = -D^{LM}_{xx} = -D^{LM}_{yy} = D^{LM}_{zz}/2. \tag{5}$$

Here, D_{LM} denotes the dipolar spin–spin coupling constant associated with the L–M atom pair. The equilibrium values of the DCT tensor are entirely defined by the equilibrium structure employed (i.e., there are no electronic contributions).[53] Vibrational corrections to both SRT and DCT were determined at the ae-CCSD(T)/cc-pCVQZ level for N_2H^+ and HCO^+ and at the ae-CCSD(T)/cc-pwCVQZ level for HCS^+ and PNH^+.

All calculations presented in this section were carried out using the CFOUR program package,[56,57] with the exception of the preliminary computations at the DFT level, which were performed using the Gaussian 16A.03 suite of programs.[58]

B. Gas-phase reactivity

The gas-phase reactions considered in this work are the protonation of PN by $H_3{}^+$ and the ion–neutral PH + NH^+ and PH^+ + NH reactions. These have been investigated using DFT. More in detail, the associated PESs were explored at the revDSD/jun(T+d)Z level of theory. As above, DFT quantum chemical calculations were performed using the Gaussian 16A.03 suite of programs.[58]

In the reactive PES, both minima and transition states (TSs) were identified, and their connectivity was confirmed via intrinsic reaction coordinate (IRC) analysis.[59] For two shallow TSs, namely ^{2}TS1 and ^{2}TS5 of Fig. 4, the IRC analysis was not feasible, and the connection was verified by performing scans (using small displacements) along the imaginary-frequency mode, followed by geometry optimization to confirm the convergence. Unless otherwise stated, the energy values reported and discussed in this article incorporate the zero-point vibrational energy (ZPE) correction, which has been computed at the revDSD/jun(T+d)Z level, within the harmonic approximation. The relative energies of the reactants, stationary points, and products of each PES presented in this study are reported in Table S1 of the supplementary material. Based on prior benchmarks,[60,61] revDSD/jun(T+d)Z electronic energies are expected to be accurate to within ~10 kJ/mol relative to higher-level CC-based composite approaches (e.g., junChS[62]). Based on the literature on this topic,[63,64] we performed junChS single-point calculations—using the same protocol adopted for third-row species in Ref. 61—on representative stationary points of the PESs. The resulting deviations with respect to revDSD/jun(T+d)Z lie within the accuracy range mentioned above and do not significantly affect the energetics or the reaction rates reported here. As a compromise between efficiency and accuracy, the junChS calculations were not extended to the full PESs, restricting them to these representative points. When computed, the corresponding junChS values are reported in the main text.

The protonation reaction involves two reactants that are singlet species; consequently, only its singlet reactive PES has been considered. The PH + NH^+ and PH^+ + NH processes occur between a doublet and a triplet species, thus resulting in two possible spin surfaces, doublet and quartet, which have been investigated. For the sake of clarity, stationary points on the doublet and quartet PESs are labeled with a superscript indicating the spin multiplicity (e.g., ^{2}**TS** and ^{4}**TS**, respectively), while no superscript is used for singlet stationary points.

Capture rate coefficients were computed for the three reactions mentioned above by employing the approach developed by Klippenstein and Georgievskii.[65,66] While a detailed account is available in Refs. 65 and 66, a brief overview of the model is provided here below. This approach uses a classical framework based on a modified version of transition state theory (TST), which has been adapted to describe long-range capture dynamics that prevails at low temperatures. The temperature range considered in this work spans from 10 to 400 K, thus covering the temperatures relevant for most interstellar sources. The method relies on a long-range interaction potential that incorporates three contributions: charge–dipole, charge–quadrupole, and charge–induced dipole. Since we consider only ion–neutral reactions where the neutral reactant is a diatomic molecule, the resulting long-range potential is given by

$$V(R,\theta) = -\frac{\mu q}{R^2}\cos\theta + \frac{Qq}{4R^3}(3\cos^2\theta - 1) - \frac{q^2(\alpha_\parallel \times \cos^2\theta + \alpha_\perp \times \sin^2\theta)}{2R^4}. \tag{6}$$

Here, R is the distance between the centers-of-mass of the two reactants, θ is the angle between the neutral molecule's internuclear axis and the line connecting the two centers-of-mass, and q is the ionic charge (equal to +1 in all the reactions studied here). The dipole moment μ, quadrupole moment Q, and polarizability tensor components $\alpha_\parallel = \alpha_{zz}$ and $\alpha_\perp = \alpha_{xx} = \alpha_{yy}$ refer to the neutral reactant. The temperature-dependent capture rate coefficient $k(T)$ is then evaluated using the following formalism:

$$k(T) = \frac{\sqrt{8\pi}\; m_r^{-1/2}T^{-\nu/2}}{\Gamma(\nu/2 - 1/2)}\int_0^{+\infty} dEe^{-E/T}\int_0^{+\infty} dXN_x^\dagger(E,X), \tag{7}$$

where

$$X = \frac{J^2}{2m_r}, \tag{8}$$

$$N_x(E,X|R) = \langle[E - V(\theta,R) - X/R^2]\rangle_\theta, \tag{9}$$

$$N_x^\dagger(E,X) = \min_R\{N_x(E,X|R)\}, \tag{10}$$

where m_r is the reduced mass of the ion–neutral system, Γ is the gamma function with $\Gamma(n) = (n-1)!$, T is the temperature, E is the energy, and ν is the number of degrees of freedom of the system: $\nu = 3 + \nu_{rot,1} + \nu_{rot,2}$, accounting for the translational and rotational contributions of both reactants. The variable J is the total angular momentum of the system. For each value of X (and thus J), the distance R that minimizes $N_x(E,X|R)$ was selected, as specified in Eq. (10). The integrals over E, X, and θ were evaluated numerically using low-dimensional phase space integrations. Angular averaging, as described by Eq. (9), was performed employing a Monte Carlo sampling of 10^3 points over the range $\theta \in [0, 2\pi]$, and the minimization of N_x with respect to R was carried out with a step size of 0.05 bohr. The energy and X grid parameters were adapted at each temperature to ensure accurate integration over the relevant domain, while maintaining computational efficiency. The resulting capture rate coefficients are obtained in atomic units. To assess the impact of each interaction contribution, single-term potentials were also considered, and their corresponding capture rates were computed numerically. In single-term cases, the numerical integration was validated against analytical results,[65] confirming the reliability of the approach.

The PESs explored in this study exhibit several accessible reaction pathways following the initial capture step. The branching ratios among these pathways were determined from the corresponding global rate constants that, in turn, were obtained for the resolution of the master equations. For this task, the MESS software package[67,68] was used. Global rate constants were calculated over the 10–400 K temperature range at a pressure of 1×10^{-12} atm, which represents the low-pressure limit. An energy-to-temperature resolution of 0.2 was adopted. The rigid-rotor harmonic-oscillator (RRHO) model was used for both TSs and minima. For TSs, quantum tunneling was accounted for using the Eckart model.[69] For the exit channels, depending on the final stationary point, a combination of relaxed and rigid scans was employed to map the reaction coordinate toward the products, without identifying significant energy barriers. The resulting scan energy profiles were then fitted using an analytical form derived from the Phase Space Theory (PST) for ion–neutral interactions. The adopted fitting function is

$$f(R) = f(R = 10\,\text{Å}) + C/R^4, \tag{11}$$

where R is the separation distance and C is the PST constant. A distance of 10 Å is commonly assumed to represent non-interacting fragments, a value supported here by the comparison with the sum of the energies for infinitely separated fragments. The C constants were then used in the input file of MESS to describe the exit channels within the PST formalism. Stationary point energies supplied to MESS were taken from the revDSD/jun(T+d)Z calculations described above.

The values of the rate coefficients for both the long-range interaction, modeled with the three-term potential, and the reaction pathways as a function of temperature are reported in Table S2 of the supplementary material. Finally, the global reaction rates at different temperatures were fitted using the three-parameter Arrhenius–Kooij formula,[70]

$$k(T) = \alpha\left(\frac{T}{300}\right)^{\beta} \exp\left(-\frac{\gamma}{T}\right), \tag{12}$$

where T is expressed in K and α, β, and γ are the fitted parameters.

III. RESULTS AND DISCUSSION

In analogy to the presentation of the computational methodology provided in Sec. II, the topics are here addressed separately. The exploration of the electronic states of protonated PN is presented first. This is followed by the spectroscopic characterization, reported together with the results for the three well-studied cations, N_2H^+, HCO^+, and HCS^+, that allow us to understand the accuracy obtained for the spectroscopic parameters of PNH^+. Then, we present possible formation pathways of this ion under interstellar conditions, reporting the thermochemical and kinetic results for the three ion–molecule reactions considered. Finally, we present the implementation of these reactivity insights into a dedicated astrochemical network.

A. Electronic states of protonated PN

A reliable spectroscopic characterization, especially in the field of astrochemistry, requires identifying the low-lying structures of the molecular species of interest. Several theoretical studies have investigated the electronic structures of protonated PN. In 1993, Glaser *et al.*,[71] based on CISD/6-31G* calculations, predicted that the PNH^+ isomer in the singlet $^1\Sigma^+$ state lies ~400 kJ/mol below its HPN^+ isomer in the singlet $^1\Sigma^+$ state. They also estimated the proton affinity (PA) of PN when forming singlet PNH^+ to be around 800 kJ/mol. Similar results regarding structures, energies, and PA values for both singlet isomers were reported earlier by Maclagan[72] and in the pioneering work of Buenker *et al.*[73] Su *et al.*[74] explored the protonation of various heterodiatomics using several computational approaches, including MP2/6-31G**. Their study placed the singlet PNH^+ 341 kJ/mol lower in energy than the singlet HPN^+, with PA values of 820 and 449 kJ/mol, respectively. In addition to singlet states, Largo *et al.*[75] investigated the triplet states of protonated PN. At the MP4/6-31G** level of theory, they found that the N-side triplet isomer, $PNH^+(3A')$, is bent and lies 390 kJ/mol above the singlet ground state $PNH^+(^1\Sigma^+)$, while the P-side triplet $HPN^+(^3A')$ is bent as well and is 600 kJ/mol higher in energy than $PNH^+(^1\Sigma^+)$. Experimental studies remain instead scarce; however, in 1990, Adams *et al.*[76] measured a PA of 799 ± 8 kJ/mol for PN, in good agreement with the theoretical predictions for the singlet PNH^+.

Here, we present the results from DFT calculations performed at the revDSD/jun(T+d)Z level. The four electronic states of protonated PN mentioned above, namely $PNH^+(^1\Sigma^+)$, $HPN^+(^1\Sigma^+)$, $PNH^+(^3A')$, and $HPN^+(^3A')$, were examined and are shown, according to their relative energy, in Fig. 1. Among them, the lowest-energy structure corresponds to the singlet state in which the proton is bound to the N end of PN: $PNH^+(^1\Sigma^+)$. The linear singlet HPN^+ is found 350 kJ/mol higher in energy. The triplet states, $PNH^+(^3A')$ and $HPN^+(^3A')$, lie 444 and 525 kJ/mol above the singlet PNH^+, respectively. The electronic energies of the four structures were also evaluated at the junChS level of theory: relative to $PNH^+(^1\Sigma^+)$, $HPN^+(^1\Sigma^+)$, $PNH^+(^3A')$, and $HPN^+(^3A')$ lie 362, 452, and 512 kJ/mol higher, respectively. These findings are thus fully consistent with earlier conclusions. It is important to note that inconsistencies occasionally appear in the literature and astrochemistry databases, such as KIDA[77] and UMIST,[78] where the protonated form of PN is sometimes denoted as HPN^+, although most likely referring to the lowest-energy isomer. Given the possibility that both isomers exist, as seen for the analogous species HCO^+ and HOC^+,[79] we recommend that the lowest-energy form is always explicitly referred to as PNH^+.

B. Spectroscopic characterization of protonated PN

1. Equilibrium structure and rotational constant

The accuracy of the computed equilibrium rotational constant only depends on the quality of the molecular equilibrium structure. To ensure high precision, we employed the *full* composite scheme

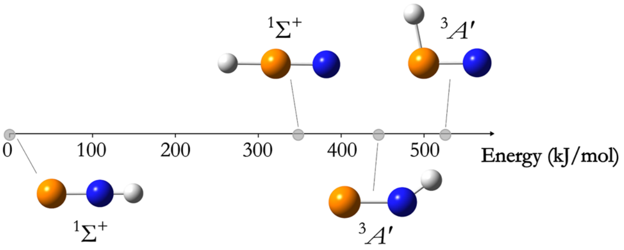

FIG. 1. Lowest singlet and triplet electronic states of protonated PN. The electronic term symbol associated with each structure is indicated. Relative ZPE-corrected energies are reported at the revDSD/jun(T+d)Z level of theory.

introduced in Sec. II. As already mentioned, to assess the accuracy of our approach for PNH^+, the same methodology has been applied to three well-characterized isovalent species: N_2H^+, HCO^+, and HCS^+. These three ions have been extensively studied by high-resolution rotational spectroscopy, and their rotational constants are thus known with great precision. Table I presents the computed equilibrium structures and rotational constants for the four protonated ions, obtained at various levels of composite schemes: CBS, CBS+CV, CBS+CV+fT, and CBS+CV+fT+fQ. For all species, interatomic distances vary from one level of theory to the other, with differences ranging from less than 0.0001 to ~0.005 Å. Moving from CBS to CBS+CV+fT+fQ, the overall change in the bond distance ranges from 0.001 to 0.003 Å. These values are small; however, it has to be noted that a variation of 0.002 Å in the interatomic distance can affect the rotational constant by several tenths of a percent,[80] which translates, for diatomic molecules, to shifts of tens to thousands of MHz in the rotational constant. Therefore, these structural variations significantly impact the ability to achieve sub-0.1% accuracy in the predicted rotational constant, which is crucial for providing effective guidance to experiment. In particular, relative to the CBS level, the CV contribution is the largest one and induces an average absolute bond decrease of 0.002 Å. The fT and fQ corrections lead to further shifts of −0.0004 Å with respect to CBS+CV and +0.0007 Å relative to CBS+CV+fT, respectively. From the equilibrium geometries, the equilibrium rotational constants B_e are straightforwardly derived. It is worth highlighting that the equilibrium structures obtained here are in good agreement with previous studies. For N_2H^+ and HCO^+, the bond lengths predicted using the *full* composite scheme differ by only ~0.0001 Å from the semi-experimental equilibrium values reported by Mladenović *et al.*[81,82] In the case of HCS^+, the derivation of a semi-experimental equilibrium structure is more challenging due to the limited number of rotationally characterized isotopologues. Nevertheless, Margulès *et al.*[83] reported best-estimated structural parameters that differ from the present results by only a few tenths of mÅ.

As detailed in Sec. II, the equilibrium rotational constants were corrected for vibrational and electronic effects. Table I also summarizes the computed ground-state rotational constants of these four cations considered, alongside their experimental counterparts. For them, we refer to the studies of Cazzoli *et al.*[84] for N_2H^+ and HCO^+ and Margulès *et al.*[83] for HCS^+. The deviation of the computed ground-state B_0^{v} (vibrational correction only) and B_0^{ve} (vibrational and electronic corrections) constants from experiment varies in sign across the species. The average absolute deviation for the three reference cations is 0.0070% when only vibrational corrections are considered and 0.0063% when electronic effects are also included. In the specific case of HCO^+, including the electronic correction slightly increases the deviation (by 0.08 MHz), but

TABLE I. Computed equilibrium structures of N_2H^+, HCO^+, HCS^+, and PNH^+ at different levels, along with their corresponding equilibrium rotational constants. The equilibrium and ground-state rotational constants obtained using the *full* composite scheme are compared with experiment. Boldface denotes the best data of PNH^+ to be used for supporting experimental investigations or replace them.

Species	Parameter	CBS[a]	CBS+CV[b]	CBS+CV+fT[c]	*full*[d]	B_0^{v}(*full*)[e]	B_0^{ve}(*full*)[f]	B_0(expt.)[g]
N_2H^+	r(N–N) (Å)	1.094 2	1.092 3	1.091 6	1.093 0			
	r(N–H) (Å)	1.034 2	1.033 3	1.033 0	1.033 3			
	B_e (MHz)	46 731.42	46 882.55	46 933.26	46 830.97	46 589.52	46 588.77	46 586.875 49(18)
	$\lvert\delta_{exp}\rvert$[h]				[0.52%]	[0.005 7%]	[0.004 1%]	
HCO^+	r(C–O) (Å)	1.107 3	1.105 2	1.105 1	1.105 7			
	r(C–H) (Å)	1.093 4	1.092 2	1.092 2	1.092 1			
	B_e (MHz)	44 707.16	44 860.26	44 872.89	44 828.93	44 590.02	44 589.94	44 594.428 66(16)
	$\lvert\delta_{exp}\rvert$[h]				[0.53%]	[0.009 9%]	[0.010 1%]	
HCS^+	r(C–S) (Å)	1.479 0	1.475 3	1.475 0	1.476 0			
	r(C–H) (Å)	1.082 1	1.080 8	1.080 6	1.080 6			
	B_e (MHz)	21 348.71	21 452.59	21 459.94	21 434.34	21 335.99	21 336.14	21 337.140 71(66)
	$\lvert\delta_{exp}\rvert$[h]				[0.46%]	[0.005 4%]	[0.004 7%]	
PNH^+	r(P–N) (Å)	1.461 0	1.457 1	1.456 3	**1.458 1**			
	r(N–H) (Å)	1.013 6	1.012 7	1.012 3	**1.012 7**			
	B_e (MHz)	20 539.27	20 644.14	20 666.93	**20 617.26**	**20 514.38**	**20 514.35**	
	$\lvert\delta_{exp}\rvert$[h]					[≈2 MHz]	[≈2 MHz]	

[a] CBS: extrapolation to the complete basis set limit.
[b] Core–valence correlation correction.
[c] f T: full treatment of triple excitations.
[d] CBS+CV+f T+fQ level, with fQ standing for full treatment of quadruple excitations.
[e] Vibrational correction added to B_e(*full*).
[f] Vibrational and electronic corrections added to B_e(*full*).
[g] Experimental values. N_2H^+: Ref. 84 ("fit 2" result). HCO^+: Ref. 84. HCS^+: Ref. 83. Uncertainties are provided in parentheses, as units of the last digit of the reported value.
[h] Absolute value of the relative deviation with respect to experiment. For PNH^+, the deviation reported corresponds to the largest relative deviation observed, at the same level, for the three other species.

the relative error remains on the order of 0.01%. Such extremely small deviations, below 0.01%, likely result from error compensation. Indeed, as shown by Puzzarini and Stanton,[80] a 0.01% change in B can correspond to a bond length variation of roughly 0.000 05 Å—approaching nuclear dimensions and thus beyond the descriptive power of standard quantum-chemical methods.

For PNH^+, the final predicted ground-state rotational constant, incorporating both vibrational and electronic corrections, is 20 514.35 MHz and is thus expected to be conservatively affected by an error of 0.01%, which means an absolute deviation of 2 MHz. Finally, it should be mentioned that previous theoretical studies have been reported in the literature for N_2H^+,[84,85] HCO^+,[84,86] and HCS^+,[87,88] employing a variety of computational approaches that include extrapolation to the CBS limit, core–valence correlation effects, and relativistic corrections. Despite these methodological differences, the present results show good agreement with the literature values, with deviations smaller than 0.05% across all species.

2. Quartic and sextic centrifugal distortion constants

To predict the rotational spectrum of PNH^+, in addition to rotational constants, centrifugal distortion terms and hyperfine parameters need to be computed. As above, the data of N_2H^+, HCO^+, and HCS^+ have been employed for benchmarking our methodology. Concerning centrifugal distortion, the quartic (D) and sextic (H) centrifugal distortion constants have been computed as detailed in Sec. II and collected in Table II, where they are compared with the available experimental values. These latter data are obtained from Cazzoli *et al.*[84] for N_2H^+ and HCO^+ and from Marguliès *et al.*[83] for HCS^+. For the quartic distortion constant, the average absolute deviation is 2%, with absolute differences remaining below 2 kHz. In the case of the sextic constant, the average deviation reaches 59%; however, this corresponds to less than 80 mHz in absolute terms. It is worth noting that for H, the experimental uncertainties often represent several tens of percent of the reported values. Therefore, the discrepancies in the theoretical predictions partly reflect these experimental errors.

TABLE II. Quartic and sextic centrifugal distortion constants of N_2H^+, HCO^+, HCS^+, and PNH^+. Absolute values of the relative deviations with respect to experiment are reported in brackets.

	D (kHz)		H (mHz)	
Species	This work[a]	Expt.[b]	This work[c]	Expt.[b]
N_2H^+	85.99[2.3%]	87.9655(44)	49.3[49%]	96(11)
HCO^+	81.16[2.0%]	82.8339(19)	59.2[24%]	77.4(58)
HCS^+	21.16[1.6%]	21.5075(21)	2.3[73%]	8.3(24)
PNH^+	**19.28**		**−0.6**	

[a] Quartic centrifugal distortion constants computed with the "CBS+CV+fT+fQ" composite method.

[b] Experimental values. N_2H^+: Ref. 84 ("fit 2" result); HCO^+: Ref. 84; HCS^+: Ref. 83. Experimental uncertainties are provided in parentheses, as units of the last digit of the reported value.

[c] Sextic centrifugal distortion constants obtained at the CCSD(T)/cc-p(w)CVQZ level of theory with all electrons included.

Compared to previous theoretical studies, the predicted D and H constants reported in Table II show a good agreement, with deviations attributable to methodological differences. For N_2H^+, HCO^+, and HCS^+, our values are within a few kHz for D and well within 1 mHz for H with respect to previous theoretical values.[84,88] The present D constants were computed from harmonic force field calculations using the *full* composite scheme, while H was obtained via anharmonic ae-CCSD(T) calculations in conjunction with quadruple-zeta basis sets. For PNH^+, we predict $D = 19.28$ kHz and $H = -0.6$ mHz, which are expected to show deviations from experiment comparable to those observed for the isovalent reference species.

3. Electric dipole moment and hyperfine parameters

Table III presents the electric dipole moment (μ) of N_2H^+, HCO^+, HCS^+, and PNH^+. Experimental data for μ are scarce. To the best of our knowledge, the only measured value is for N_2H^+, determined by Havenith *et al.*[89] from isotopic shifts. This is consistent with the *ab initio* prediction by Botschwina,[90] obtained at the CEPA-1(ED) level of theory, and also with our result. For HCO^+, our predicted value agrees well with the earlier datum by Botschwina *et al.*,[91] obtained at the CCSD(T)/cc-pVQZ level. In the case of HCS^+, our calculated dipole moment matches well with earlier theoretical predictions by Puzzarini,[87] who employed the CCSD(T)/CBS+CV composite approach, and by Botschwina and Sebald,[92] who used the CEPA-1(ED) theory level. For PNH^+, we predict a dipole moment of 0.45 D, including a vibrational correction of −0.02 D. Given the agreement with previous experimental and theoretical findings for related systems, we estimate an accuracy for our predicted value for PNH^+ of about 0.1 D.

Table IV collects the results for the hyperfine parameters: nuclear quadrupole coupling, nuclear spin–rotation, and dipolar spin–spin coupling constants for N_2H^+, HCO^+, HCS^+, and PNH^+. Concerning NQCCs, as already mentioned, the only quadrupolar nucleus is N; thus, this interaction is present only in N_2H^+ and PNH^+. For N_2H^+, the predicted NQCCs (the two N atoms being not equivalent), computed at the *full* level with vibrational corrections included, differ by ~0.05 MHz from the experimental values reported by Cazzoli *et al.*[84] and are also consistent with their theoretical predictions reported in the same work at the ae-CCSD(T)/aug-cc-pCV6Z level incorporating an

TABLE III. Electric dipole moment of N_2H^+, HCO^+, HCS^+, and PNH^+.

	μ (D)		
Species	This work[a]	Expt.[b]	Previous studies[c]
N_2H^+	3.40	3.4(2)	3.374(20)
HCO^+	3.92		3.90(1)
HCS^+	1.83		1.835(15)
PNH^+	**0.45**		

[a] Electric dipole moment computed with the "CBS+CV+fT+fQ" composite method and incorporating vibrational correction.

[b] Experimental value: Ref. 89. The uncertainty is given in parentheses as units of the last digit of the reported value.

[c] Previous theoretical values. N_2H^+: Ref. 90; HCO^+: Ref. 91; HCS^+: Ref. 87. Uncertainties are given in parentheses as units of the last digit of the reported value.

TABLE IV. Hyperfine parameters of N_2H^+, HCO^+, HCS^+, and PNH^+.

Species	Parameter	Unit	This work[a]	Expt.[b]
N_2H^+ $N^1N^2H^+$	$\chi(N^1)$	MHz	−1.397	−1.3582(29)
	$\chi(N^2)$	MHz	−5.765	−5.6903(15)
	$C(N^1)$	kHz	8.36	8.60(44)
	$C(N^2)$	kHz	11.54	11.86(31)
	$C(H)$	kHz	−5.29	<20
	$D_{N^1N^2}$	kHz	−0.48	
	D_{N^1H}	kHz	−7.14	−7.135
	D_{N^2H}	kHz	−0.89	
HCO^+	$C(H)$	kHz	−5.10	
HCS^+	$C(H)$	kHz	−2.71	
PNH^+	$\chi(N)$	MHz	**−0.809**	
	$C(P)$	kHz	**45.83**	
	$C(N)$	kHz	**3.99**	
	$C(H)$	kHz	**−2.23**	
	D_{PN}	kHz	**−1.12**	
	D_{PH}	kHz	**−3.19**	
	D_{NH}	kHz	**−7.54**	

[a] Equilibrium nuclear quadrupole coupling constants computed with the "CBS+CV+fT+fQ" composite method (see the text for details). Nuclear spin–rotation and dipolar spin–spin coupling constants obtained at ae-CCSD(T)/aug-cc-p(w)CVQZ on top of the "CBS+CV+fT+fQ" equilibrium geometry. All hyperfine parameters are vibrationally corrected at the ae-CCSD(T)/cc-p(w)CVQZ level of theory.

[b] Experimental values. N_2H^+: Ref. 84 and Ref. 93 for the $C(H)$ upper limit. Experimental uncertainties are given in parentheses as units of the last digit of the reported value.

ae-CCSD(T)/aug-cc-pCVQZ vibrational correction. For PNH^+, the predicted NQCC for N is −0.809 MHz. Based on the comparison discussed above for N_2H^+, we expect that this value is affected by an uncertainty of about 3%.

The hyperfine structure of rotational spectra is further shaped by the nuclear spin–rotation interaction and the dipolar spin–spin coupling, governed by the SRT and DCT tensors, respectively. Table IV reports the unique spin–rotation interaction (C) and dipolar spin–spin coupling (D) constants for the four ions considered, each of them containing at least one nucleus with nonzero spin, which is hydrogen (H). For all ions, the spin–rotation constants are usually very small, thus leading to very small effects (in most cases hardly resolvable) on the rotational spectrum. For N_2H^+, the predicted N spin–rotation constants deviate by less than 0.1 kHz from the theoretical values reported by Cazzoli *et al.*[84]—obtained at the CCSD(T)/aug-cc-pCV5Z level of theory with a CCSD(T)/aug-cc-pCVQZ vibrational correction—and by about 0.3 kHz from their experimental measurements. Caselli *et al.*[93] also provided an observational upper limit of 20 kHz for $C(H)$, which is consistent with theoretical predictions. For HCO^+ and HCS^+, no previous experimental or theoretical SRT data for H are available in the literature. For PNH^+, the predicted spin–rotation interaction constants are 45.83 kHz for P, 3.99 kHz for N, and −2.23 kHz for H. Table IV also lists the dipolar spin–spin coupling constants for N_2H^+ and PNH^+, the only two ions among those considered having two nuclei with nonzero nuclear spin. To the best of our knowledge, the only previous consideration of these constants concerns N_2H^+ and is the theoretical prediction by Cazzoli *et al.*[84] computed at the ae-CCSD(T)/aug-cc-pCVQZ level of theory. In that work, a value of −7.135 kHz for the interaction between N^1 (the central N atom) and H was reported, which compares very well with our prediction of −7.14 kHz, which thus deviates by less than 10 mHz from the experimental value. The remaining DCT components in N_2H^+ are predicted to be an order of magnitude smaller. For PNH^+, the computed dipolar spin–spin coupling constants are −3.19 kHz for the P–H pair, −7.54 kHz for N–H, and −1.12 kHz for P–N.

4. Vibrational fundamental frequencies of PNH^+

Knowledge of the vibrational frequencies allows the prediction of the IR spectrum. Furthermore, combined with rotational parameters, they permit the characterization of the rovibrational spectrum. As explained in Sec. II, we computed the harmonic frequencies and IR intensities of the four cations considered in this study using the *full* composite scheme. For each species, anharmonic force field calculations were performed to incorporate anharmonicity in the fundamental frequencies and the corresponding IR intensities. Whenever possible, the predicted fundamental frequencies are compared with available experimental vibrational band centers. The results are collected in Table V.

For N_2H^+, HCO^+, and HCS^+, all fundamental vibrational bands have been experimentally characterized,[94–101] with the only exception of the very weak ν_3 band of HCS^+. The average deviation from the experiment of our computed fundamental frequencies is 0.14%, with the largest discrepancy not exceeding 0.26%. In absolute terms, this means that our calculations predict the band centers with an accuracy of 1–5 cm^{-1}. For PNH^+, the anharmonic frequencies—$\nu_2 = 667.2\ cm^{-1}$ (I = 137.1 km/mol), $\nu_3 = 1389.1\ cm^{-1}$ (I = 14.0 km/mol), and $\nu_1 = 3446.9\ cm^{-1}$ (I = 383.0 km/mol)—are expected to show a similar level of accuracy.

C. Formation routes of PNH^+ relevant to astrochemistry

In analogy to all protonated species, the formation of PNH^+ can be envisioned as resulting from the protonation of pre-existing PN molecules. As mentioned in Sec. III A, the PA of PN has been measured to be ∼800 kJ/mol.[76] This large PA value implies that a variety of proton donors are thermodynamically capable of reacting with PN. However, a proper evaluation of each protonation pathway requires a detailed analysis of the corresponding PES, especially in the astrochemical context where only exothermic, barrierless reactions are favored. In this work, we have characterized the protonation of PN by the most abundant proton donor in the ISM, namely H_3^+. This reaction is already included in major astrochemical databases. For example, in the KIDA database, the protonation reaction of PN by H_3^+ is referenced, and the reaction rate is estimated using the Su–Chesnavich formalism, as described by Wakelam *et al.*,[102] in conjunction with the electric properties of PN from the work of Woon and Herbst.[103] While this approach neglects short-range interaction effects, it generally provides reasonable estimates for the overall rate of exothermic reactions. Here, we explicitly evaluate both long-range and short-range contributions of the PN + H_3^+ reaction. In particular, the possibility of isomerization between PNH^+ and HPN^+ at short range motivates a detailed

TABLE V. Harmonic and fundamental frequencies of the vibration modes of N_2H^+, HCO^+, HCS^+, and PNH^+.

Species	Mode	ω_i[a] (cm^{-1})	ν_i[a] (cm^{-1})	I[a] (km/mol)	$\nu_i^{exp.}$[b] (cm^{-1})
N_2H^+	ν_2	696.4	686.0[0.11%]	229.2	685.251 0(4)[94]
	ν_3	2296.4	2259.1[0.05%]	11.9	2257.866 7(13)[95]
	ν_1	3400.2	3227.2[0.21%]	809.5	3233.960 8(2)[96]
HCO^+	ν_2	845.1	830.4[0.26%]	75.0	828.230 5(9)[97]
	ν_3	2218.9	2189.0[0.23%]	12.8	2183.949 61(2)[98]
	ν_1	3231.4	3093.9[0.17%]	364.2	3088.739 51(31)[99]
HCS^+	ν_2	781.1	767.2[0.10%]	116.6	766.453(1)[100]
	ν_3	1427.1	1406.0	0.7	
	ν_1	3276.1	3144.0[0.07%]	256.6	3141.682 3(5)[101]
PNH^+	ν_2	678.4	**667.2**	**137.1**	
	ν_3	1409.6	**1389.1**	**14.0**	
	ν_1	3607.0	**3446.9**	**383.0**	

[a] Harmonic frequencies, ω_i, computed at the "CBS+CV+fT+fQ" level; fundamental frequencies, ν_i, and infrared intensities, (I), obtained after applying anharmonic corrections to harmonic values. Absolute relative deviations with respect to experiment are reported in brackets.

[b] Experimental uncertainties are given in parentheses as units of the last digit of the reported value.

exploration of the reaction pathway. Two additional protonation reactions are also listed in KIDA,[77] those involving H_3O^+ and HCO^+. All three protonation pathways—via $H_3{}^+$, H_3O^+, and HCO^+—are likewise included in the UMIST database.[78] In specific P-oriented astrochemical networks, such as those used in Ref. 14 and in the final section of this work, the additional reaction between PN and H_2O^+ is also included, following the work of MacKay and Charnley.[104] Here, we focus on the dominant route involving $H_3{}^+$. It is important to note that each of these four reactions requires the presence of pre-existing PN molecules. To explore alternative formation mechanisms that bypass the need for PN itself, we investigate two new reactions: PH + NH^+ and PH^+ + NH. Both processes can lead to protonated PN without requiring prior formation of PN. While only NH has been detected in the ISM to date,[105] all these four species are commonly included in astrochemical network models and may contribute to the interstellar formation of protonated PN. As mentioned in Sec. II, for each reaction, the PES has been explored at the revDSD/jun(T+d)Z level of theory, capture rate coefficients evaluated using a long-range interaction model based on a three-term potential, and the branching ratios within each process derived via master equation simulations.

1. Protonation reaction of PN by $H_3{}^+$

Due to the high abundance of $H_3{}^+$ in the ISM and the relatively low proton affinity of H_2, the protonation of neutral molecules by $H_3{}^+$ is among the primary mechanisms for the formation of protonated species in space. Figure 2 shows the PES associated with the reaction between PN, in its electronic ground state ($^1\Sigma^+$),[106] and $H_3{}^+$. Two product channels are identified: $PNH^+(^1\Sigma^+)$ + H_2 and $HPN^+(^1\Sigma^+)$ + H_2, the bimolecular products lying 369 and 19 kJ/mol below the reactants, respectively.

The reaction begins with the barrierless formation of **Min1**, the lowest-energy minimum on the PES (−375 kJ/mol), corresponding to a complex of the form $PNH^+\cdots H_2$. From **Min1**, the system

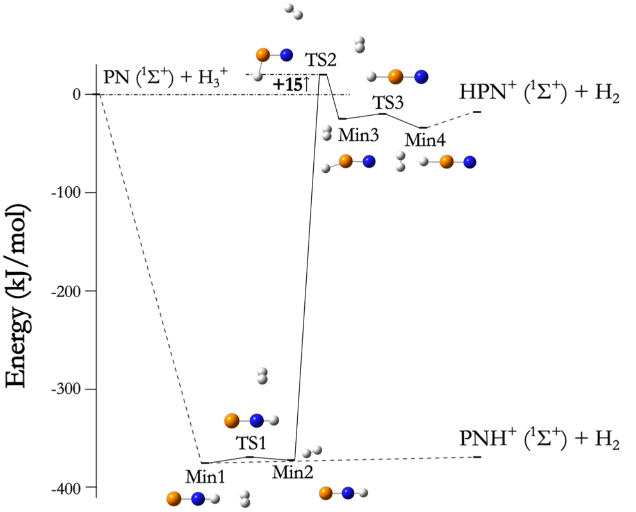

FIG. 2. Singlet PES of the PN + $H_3{}^+$ reaction. Relative ZPE-corrected energies (with respect to reactants; Table S1) are at the revDSD/jun(T+d)Z level of theory.

can proceed through an exit pathway to form $PNH^+(^1\Sigma^+)$ + H_2. Alternatively, it may access **Min2** (2 kJ/mol above **Min1**) via **TS1** (5 kJ/mol above **Min1**), where the H_2 moiety shifts toward the P end of PNH^+. **Min2** connects to a pathway leading to the formation of the HPN^+ isomer. This route proceeds via the emerged **TS2** (15 kJ/mol above the reactants) to **Min3** (−25 kJ/mol), where both H^+ and H_2 are localized on the P side of PN. Subsequently, overcoming **TS3** (−24 kJ/mol) leads to **Min4** (−34 kJ/mol), a complex of the form $H_2\cdots HPN^+$, and eventually to the HPN^+ + H_2 products. At low interstellar temperatures, where only exothermic reactions with barrierless reactants' approach and entirely submerged channels are efficiently accessible, this PES analysis indicates that the formation of $PNH^+(^1\Sigma^+)$ is strongly favored over the formation of its isomer HPN^+ in the reaction between PN and $H_3{}^+$.

Figure 3 presents the temperature dependence of the capture and reaction rate coefficients for the gas-phase PN + $H_3{}^+$ process. Evaluation of the capture rate requires knowledge of the electric properties for the neutral reactant, in this case PN. The electric dipole moment adopted for PN is 1.08 a.u., based on the measurements performed by Hoeft *et al.*[107] and Raymonda and Klemperer,[108] as suggested in the Cologne Database for Molecular Spectroscopy (CDMS) database.[109] The quadrupole moment was calculated to be −1.23 a.u. at the revDSD/jun(T+d)Z level of theory. The molecular polarizabilities, computed at the same level, result to be $\alpha_\perp = 37.01$ a.u. and $\alpha_\parallel = 24.22$ a.u.

Figure 3(a) shows the temperature-dependent capture rate as obtained using the long-range model presented in Sec. II. For comparison, the capture rates computed from the corresponding one-term potentials are also plotted. In the low-temperature regime (below 400 K), the dominant contribution arises from the charge–dipole interaction. This explains why only the approach of $H_3{}^+$ to the N-end of PN is considered in Fig. 2. The charge–induced dipole interaction becomes increasingly important when increasing the temperature. To derive the reaction rate, a so-called dynamical factor of 0.9 is applied to the long-range rate, as suggested by Klippenstein, Georgievskii, and McCall in Ref. 66 for similar ion–molecule reactions based on the comparison of the model with trajectory simulations. This factor accounts for the small fraction of trajectories that, after crossing the transition state dividing surface, revert to reactants without reaching the strong interaction region.

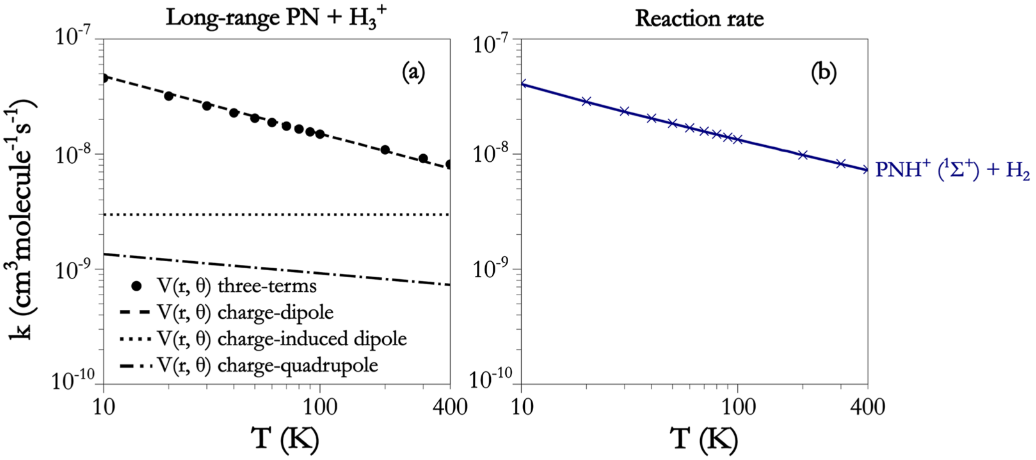

FIG. 3. (a) Temperature dependence of the long-range interaction for PN + $H_3{}^+$: the results from the three-term potential (black circles) and from the three single types of long-range interaction (black curves) are shown. (b) Temperature dependence of the reaction rate for the formation of $PNH^+(^1\Sigma^+) + H_2$ (for details, see the text). The solid line represents the Arrhenius–Kooij fit (the corresponding parameters are provided in Table VI).

TABLE VI. Arrhenius–Kooij fit parameters (α, β, and γ) for the temperature-dependent rate coefficients, $k(T)$, of the reactions investigated in this work.

Reactants	→	Products	$k(T) = \alpha\left(\frac{T}{300}\right)^\beta \exp\left(-\frac{\gamma}{T}\right)$		
			α (cm^3 $molecule^{-1}$ s^{-1})	β	γ (K)
PN + $H_3{}^+$	→	**$PNH^+(^1\Sigma^+) + H_2$**	**8.17×10^{-9}**	**−0.443**	**−1.08**
PH + NH^+	→	$PNH^+(^1\Sigma^+)$ + H	4.40×10^{-10}	−0.167	−3.73
	→	$PNH^+(^3A')$ + H	8.98×10^{-10}	−0.168	−3.70
		Total PNH^+	**1.34×10^{-9}**	**−0.167**	**−3.75**
	→	$HPN^+(^1\Sigma^+)$ + H	5.50×10^{-11}	−0.161	3.86
	→	$HPN^+(^3A')$ + H	9.10×10^{-11}	−0.162	−3.81
		Total HPN^+	**1.46×10^{-10}**	**−0.160**	**−3.87**
PH^+ + NH	→	$PNH^+(^1\Sigma^+)$ + H	7.87×10^{-10}	−0.445	−1.03
	→	$PNH^+(^3A')$ + H	1.58×10^{-9}	−0.443	−1.08
		Total PNH^+	**2.36×10^{-9}**	**−0.444**	**−1.08**

Figure 3(b) presents the temperature dependence of the reaction rate for the formation of $PNH^+(^1\Sigma^+)$ + H_2, which—as shown in Fig. 2—is the only accessible bimolecular product of this reaction under interstellar conditions. Over the 10–400 K range, the temperature dependence of the rate coefficient is well described by the Arrhenius–Kooij formula [Eq. (12)], whose fitted parameters are reported in Table VI. Our model yields k values slightly larger than those reported in the KIDA database,[77] based on the work of Woon and Herbst,[103] for the PN + $H_3{}^+$ reaction, but remains in good overall agreement. For instance, at 30 K, a rate coefficient of 2.18×10^{-8} cm^3 $molecule^{-1}$ s^{-1} is reported in the KIDA database, while our model results in a value of 2.33×10^{-8} cm^3 $molecule^{-1}$ s^{-1}.

2. Reactions between PH and NH^+ and between PH^+ and NH

In addition to the protonation reaction involving a pre-existing PN molecule, as already mentioned, the formation of PNH^+ can also result from ion–molecule reactions that do not include PN as a reactant. In this work, we have studied the PH + NH^+ and PH^+ + NH reactions. The capture rates for these two reactions differ from each other primarily for the different neutral reactants. However, once capture is demonstrated to be efficient, the two reactions evolve on the same PES. All species are considered in their electronic ground states: $^3\Sigma^-$ for PH and NH and $^2\Pi$ for PH^+ and NH^+. Therefore, as mentioned in Sec. II, doublet and quartet PESs are accessible and have been both investigated. The two reactant asymptotes are separated by 322 kJ/mol, with the PH + NH^+ pair lying higher in energy and used as the reference.

The doublet and quartet reactive PESs are shown in Figs. 4 and 5, respectively. Starting from the doublet PES (Fig. 4), three possible pathways have been found: two of them leading to $PNH^+(^1\Sigma^+)$ + H, at −748 kJ/mol, and one forming $HPN^+(^1\Sigma^+)$ + H, at −398 kJ/mol. Therefore, both products are exothermic. The three pathways differentiate from the intermediate denoted as ^{2}**Min1**, while the two barrierless entrance channels, from the approach of the two pairs of reactants, both lead to the formation of a van der Waals (vdW) complex, ^{2}**VdW**, located 353 kJ/mol below the reference. This well evolves, via a shallow TS (^{2}**VdW-TS**) whose equilibrium electronic energy is approximately only 1 kJ/mol above the vdW well, into ^{2}**Min1**, which lies 819 kJ/mol below the reference. In ^{2}**Min1**, the P–N bond is formed with one H atom positioned on each side of the system. From ^{2}**Min1**, three TSs are accessible: ^{2}**TS1**, ^{2}**TS2**, and ^{2}**TS4**, located at −749, −728, and −507 kJ/mol, respectively. ^{2}**TS1** corresponds to the migration of a H atom from the P-side to the N-side, leading to ^{2}**Min2** (−751 kJ/mol), a linear complex of the form $PNH^+\cdots H$, from which a barrierless exit channel leads to $PNH^+(1\Sigma^+)$ + H. ^{2}**TS2** connects ^{2}**Min1** to ^{2}**Min3** (−961 kJ/mol), the global minimum of the PES, and corresponds again to a H-migration from the P- to the N-side. ^{2}**Min3** has C_{2v} symmetry, and, from it, the system evolves, via ^{2}**TS3** (−698 kJ/mol), into the linear ^{2}**Min2**, again leading to $PNH^+(^1\Sigma^+)$ + H. Finally, ^{2}**TS4** rules the migration of an H atom from the N- to the P-side, thus forming ^{2}**Min4** (−629 kJ/mol), another C_{2v} minimum where both H atoms are on the P-side. Finally, ^{2}**TS5** (235 kJ/mol above ^{2}**Min4**) links this pathway to a barrierless exit channel that forms $HPN^+(^1\Sigma^+)$ + H. In conclusion, on the doublet PES, both isomeric forms of protonated PN are thermodynamically accessible from either reactant pair at low temperatures.

Figure 5 shows the quartet PES. In analogy to the doublet PES, the two pairs of reactants form, without any barrier, the same vdW complex (^{4}**VdW**), which is located at −359 kJ/mol, ~5 kJ/mol below its doublet analog. ^{4}**VdW** evolves, via ^{4}**VdW-TS** (equilibrium energy 1 kJ/mol above ^{4}**VdW**), into ^{4}**Min1**, located at −550 kJ/mol. From this intermediate, two different channels originate. The structure of ^{4}**Min1** is similar to that of ^{2}**Min1**, with the P–N bond forming and one H atom residing on each side of the PN moiety. The two TSs giving access to the two identified pathways are ^{4}**TS1** and ^{4}**TS2**, located at −372 and −341 kJ/mol, respectively, thus being submerged with

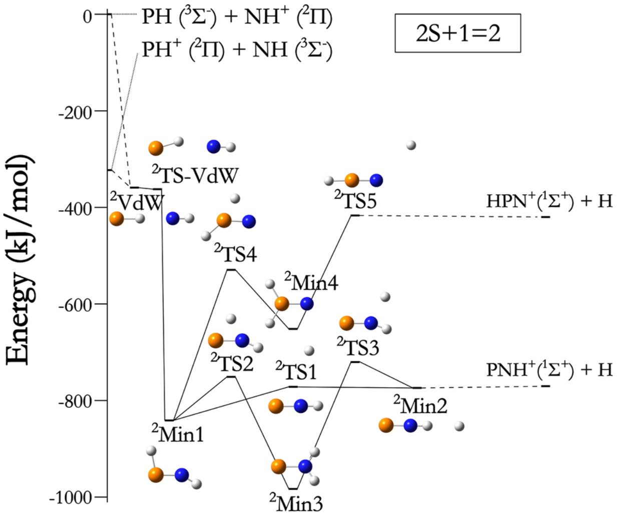

FIG. 4. Doublet PES of the PH + NH^+ and PH^+ + NH reactions. Relative ZPE-corrected energies (with respect to reactants; Table S1) are at the revDSD/jun(T+d)Z level of theory.

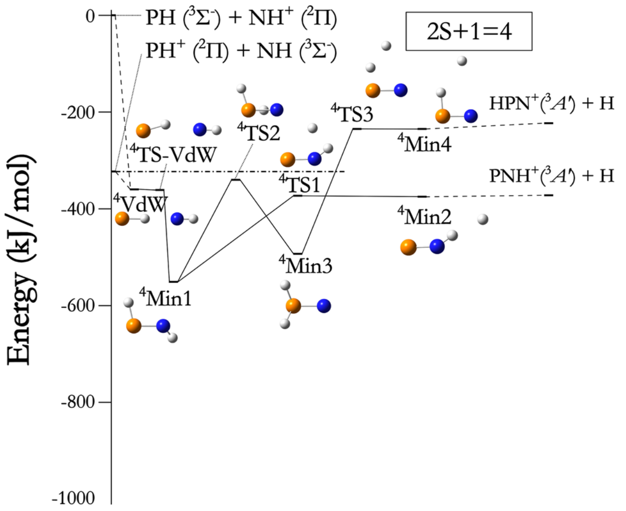

FIG. 5. Quartet PES of the PH + NH^+ and PH^+ + NH reactions. Relative ZPE-corrected energies (with respect to reactants; Table S1) are at the revDSD/jun(T+d)Z level of theory.

respect to both reactant pairs. ^{4}**TS1** governs the migration of an H atom from the P- to the N-side, leading to ^{4}**Min2** (−375 kJ/mol). From this structure, the system can proceed to form the bimolecular product $PNH^+(^3A')$ + H, which lies 371 kJ/mol below the reference and 49 kJ/mol below the energy of the PH^+ + NH reactants. Due to its proximity to the PH^+ + NH entrance channel, the pathway leading to $PNH^+(3A')$ was used to check the accuracy of the electronic energies (see Sec. II). Relative to PH^+ + NH, the revDSD/jun(T+d)Z [junChS] energies for ^{4}**VdW**, ^{4}**VdW-TS**, ^{4}**Min1**, ^{4}**TS1**, and ^{4}**Min2** are −36 [−35], −40 [−39], −228 [−229], −50 [−59], and −52 [−61] kJ/mol, respectively. ^{4}**TS2** corresponds to the migration of the N-side H and leads to ^{4}**Min3** (−493 kJ/mol), which has both H atoms bonded to the P-side. ^{4}**Min3** interconverts, via ^{4}**TS3** (−234 kJ/mol), to ^{4}**Min4** (−234 kJ/mol). From this, a barrierless exit channel forms the bimolecular product $HPN^+(^3A')$ + H, located 223 kJ/mol below the reference, but above the PH^+ + NH reactants. In conclusion, on the quartet PES, both products are thermodynamically accessible from the PH + NH^+ entrance channel, whereas only the pathway leading to $PNH^+(^3A')$ from PH^+ + NH is open under interstellar conditions.

a. Reaction rates of PH + NH$^+$*.* For the PH + NH^+ reaction, all the pathways described above are completely submerged, and the PNH^+ + H product is strongly exothermic. Therefore, all the four investigated forms of protonated PN (see Fig. 1) are thermodynamically accessible under interstellar conditions. To determine the temperature dependence of reaction rates and branching ratios of these species, the capture rate needs to be first evaluated. As in Sec. III C 1, the long-range capture theory employed here requires knowledge of the electric properties of the neutral reactant, which is, in this case, PH. To the best of our knowledge, no experimental data are available for these properties. The values used in this study were computed at the revDSD/jun(T+d)Z level of theory and include a dipole moment of 0.18 a.u., a quadrupole moment of 0.07 a.u., and polarizabilities of $\alpha_\perp$ = 26.54 a.u. and $\alpha_\parallel$ = 29.68 a.u. The dipole moment and polarizabilities are in agreement with previous CCSD(T) calculations by Müller and Woon,[110] although no reference values for the quadrupole moment were found in the literature. Figure 6(a) shows the temperature dependence of the computed long-range rates. Below 400 K, both charge–dipole and charge–induced dipole interactions significantly contribute to the capture process. The charge–dipole term dominates at temperatures lower than 150 K, while the charge–induced dipole interaction becomes increasingly relevant at higher temperatures. These results underscore the importance of including all three long-range interactions to accurately model the capture behavior across the 10–400 K range.

Figure 6(b) reports the temperature variation of the reaction rates derived from the long-range rate using a dynamical factor of 0.9 (see Sec. III C 1). A key aspect is the partitioning of flux between the doublet and quartet PESs, which has been performed on the basis of spin statistics weights: it has been assumed that 2/3 of the total rate is due to the quartet surface and 1/3 of the total rate is due to the doublet surface. This assumption is further discussed in Sec. III C 3. Within a given PES, branching ratios of the different products have been determined by solving, for each reaction channel, the corresponding master equation (see Sec. II). The derived ratios were found to remain constant across the studied temperature range under low-pressure conditions. On the doublet PES, 89% of the reactive flux leads to $PNH^+(^1\Sigma^+)$, while the remaining 11% forms $HPN^+(^1\Sigma^+)$. Similarly, on the quartet PES, 91% of the flux yields $PNH^+(^3A')$ and 9% leads to the formation of $HPN^+(3A')$. These four individual reaction rates are shown in Fig. 6(b), with the cyan color being used for PNH^+ and orange for HPN^+. Under interstellar conditions, most triplet products can be expected to undergo intersystem crossing (ISC) to their corresponding singlet states before further interaction with other particles or radiation. Under this assumption, the total reaction rates for PNH^+ and HPN^+—also shown in Fig. 6(b) in blue and red, respectively—can be interpreted as effective formation rates of the singlet species. The temperature dependence of rate coefficients is well described by the

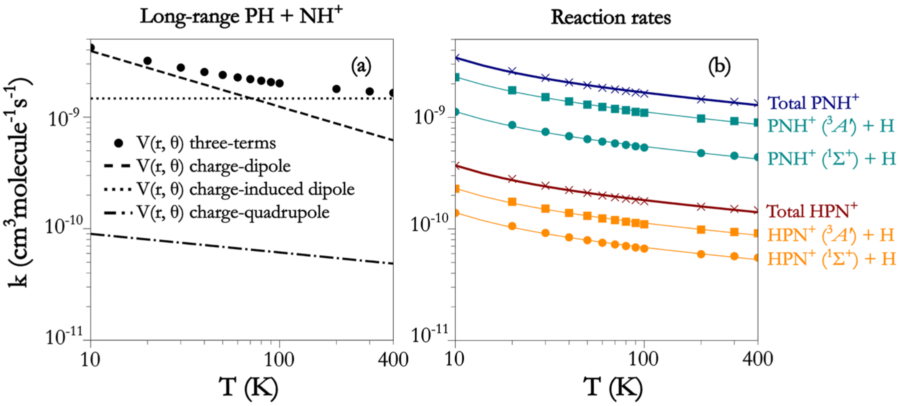

FIG. 6. (a) Temperature dependence of the long-range interaction for PH + NH^+: the results from the three-term potential (black circles) and from the three single types of long-range interaction (black curves) are shown. (b) Temperature dependence of the reaction rates for the formation of protonated PN on the doublet (cyan circles for PNH^+ and orange circles for HPN^+) and quartet (cyan squares for PNH^+ and orange squares for HPN^+) PESs (for details, see the text). The temperature behavior of the total reaction rates (blue crosses for PNH^+ and red crosses for HPN^+), corresponding to the sum of the contributions from the two PESs, is also shown. The solid lines are the Arrhenius–Kooij fits (the corresponding parameters are provided in Table VI).

Arrhenius–Kooij equation, with the parameters given in Table VI. At 30 K, the total reaction rate associated with PNH^+ corresponds to 2.30×10^{-9} cm^3 $molecule^{-1}$ s^{-1}, while the one associated with HPN^+ is 2.03×10^{-10} cm^3 $molecule^{-1}$ s^{-1}.

b. Reaction rates of PH^+ + NH. The same methodology as above was applied to the reaction between PH^+ and NH. The electric dipole moment of NH has been measured by Irwin and Dalby,[111] who reported a value of 0.54 a.u., which was the one used in our model. For the quadrupole moment and polarizabilities, values computed at the revDSD/jun(T+d)Z level of theory were employed: $Q = 0.24$ a.u., $\alpha_\perp = 10.01$ a.u., and $\alpha_\parallel = 8.75$ a.u. The resulting capture rate and how it varies with temperature are shown in Fig. 7(a). Similarly to the PN + $H_3{}^+$ case, below 400 K, the capture rate is dominated by the charge–dipole interaction, while at higher temperatures, the charge–induced dipole becomes increasingly significant. Applying the same correction factor of 0.9 employed for the two other reactions considered to account for dynamical effects leads to the total reaction rate.

Figures 4 and 5 report the doublet and quartet PES, respectively, for the PH^+ + NH reaction. As already discussed, for the doublet PES, all pathways are entirely submerged and all products are exothermic. Therefore, the formation of both singlet products, $PNH^+(^1\Sigma^+)$ and $HPN^+(^1\Sigma^+)$, is thermodynamically accessible. However, master equation calculations reveal that pathways leading to HPN^+ account for less than 0.03% of the doublet unimolecular flux. Consequently, the formation of the N-protonated isomer (PNH^+) is strongly favored. On the quartet PES, only the pathway forming triplet PNH^+ is exothermic for this reactant pair. The competing channel, leading to triplet HPN^+, involves the high-energy transition state **^{4}TS3**, which lies more than 85 kJ/mol above the entrance channel, and, therefore, the corresponding barrier can be overcome only via tunneling effects under interstellar conditions. The two reaction rates associated with the formation of singlet and triplet PNH^+ and how they vary with temperature are presented in Fig. 7(b), both plotted using the cyan color. The rate coefficients corresponding to the doublet pathway toward singlet HPN^+ are below the plot scale, their order of magnitude being 10^{-13} cm^3 $molecule^{-1}$ s^{-1} (see Table S2 of the supplementary material). The temperature dependence of the total PNH^+ reaction rate (blue solid curve) is also plotted. Under the assumption that the triplet form of PNH^+ will undergo ISC to the singlet ground state under interstellar conditions, this total coefficient effectively represents the formation rate of $PNH^+(^1\Sigma^+)$ via the PH^+ + NH reaction. The rates are well described by the Arrhenius–Kooij equation, and the corresponding parameters are reported in Table VI. At 30 K, the total PNH^+ reaction rate corresponds to 6.06×10^{-9} cm^3 $molecule^{-1}$ s^{-1}.

3. Discussion

The results presented here for the PH + NH^+ and PH^+ + NH reactions should be interpreted with some caution regarding possible ISC. The assumption of equiprobable spin states can be debated. Indeed, the entrance regions of the doublet and quartet PESs are close in energy, with the vdW wells and associated TSs separated by only a few kJ/mol. While the evolution along exothermic PESs is generally favored over spin-forbidden processes, a more detailed investigation of possible ISC during the entrance channel might potentially alter the partitioning between reactions occurring on the doublet and quartet surfaces. However, even if ISC phenomena would affect the branching between spin surfaces during the capture and vdW phases, the overall formation rate of the singlet states would not be modified. This is because we considered that most triplet products formed under interstellar conditions are expected to relax to their corresponding singlet counterparts via ISC before any further interaction occurs. Concerning the unimolecular portions of the PES, no stationary points appear sufficiently close in energy to facilitate ISC. However, only a dedicated search for potential Minimum Energy Crossing Points (MECPs) can confirm this unambiguously. The presence of exothermic product channels on both spin surfaces further reduces the driving force for ISC during the unimolecular evolution. As a result, ISC within this region of the PES is considered negligible in the present work.

In addition to enabling ISC between spin surfaces of different multiplicities, spin–orbit coupling (SOC) splits the doublet ground states of the open-shell reactants NH^+ and PH^+ into fine-structure components. At relatively high temperatures, both components are similarly populated, whereas at very low temperatures, the lower component becomes increasingly favored. These components differ in their spin–orbit coupling and associated long-range interaction parameters, which can subtly modify the capture dynamics and hence the reaction rates. Prior studies [e.g., for $C^+(^2P)$ + HCl by Dateo and Clary[112]] show that including such fine-structure effects can slightly influence capture rates while preserving their overall order of magnitude. The capture model employed in this work is spin-free and, therefore, neglects these effects.

Beyond the mechanistic considerations, the reactions presented here demonstrate that the formation of protonated PN should not be regarded solely as the result of protonation of pre-existing PN. It can also arise from alternative pathways involving the phosphinidene radical, PH, and the imidogenium cation, NH^+, or between the imidogen radical, NH, and the phosphinidynium cation, PH^+. Once formed, PNH^+ may undergo dissociative recombination reactions, potentially yielding neutral PN and thereby impacting its interstellar abundance. A dedicated study of these recombination pathways is needed to quantitatively assess the role of PNH^+ in PN formation. Moreover, the high PA (800 kJ/mol) of PNH^+ makes it a poor proton donor to most neutral molecules, thus allowing it to retain its extra proton for longer timescales than other protonated species. While dissociative recombination, fragmentation, or even proton transfer can still occur, this relative stability enhances the likelihood of PNH^+ participating in further reactions, thereby increasing the complexity of P-based chemistry in interstellar environments.

D. Astrochemical model

Here, we have implemented the reaction rates studied in Sec. III C into an astrochemical model using the code UCLCHEM.[113] We used the P chemistry network used in Refs. 14 and 114, which was an update of the one built in Ref. 115. The initial elemental abundances considered were initially taken from Asplund *et al.*,[116] except for P, Mg, Si, Cl, and F, which are depleted by factors between 5.4 and 5700. In the case P, its elemental abundance is depleted by a factor of 100 with respect to its solar value ($P/H = 2.57 \times 10^{-7}$), which has been adjusted to explain the observed abundances

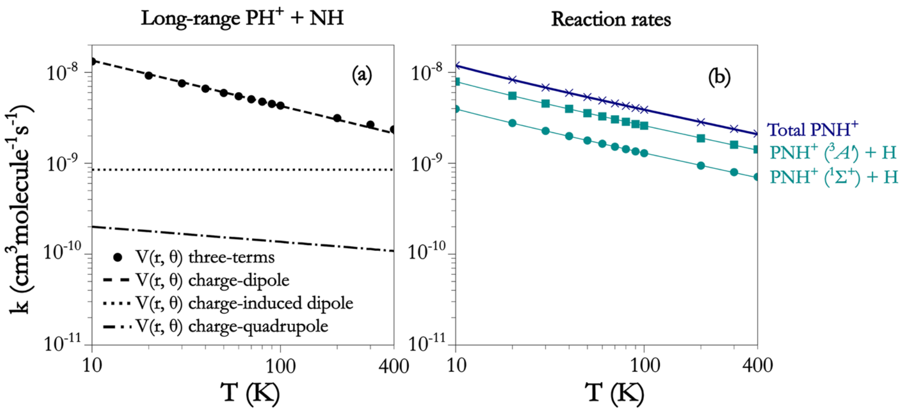

FIG. 7. (a) Temperature dependence of the long-range interaction for PH^+ + NH: the results from the three-term potential (black circles) and from the three single types of long-range interaction (black curves) are shown. (b) Temperature dependence of the reaction rates for the formation of PNH^+ on the doublet (cyan circles) and quartet (cyan squares) PES (for details, see the text). The temperature behavior of the total reaction rate (blue crosses), corresponding to the sum of the contributions from the two PESs, is also shown. The solid lines are the Arrhenius–Kooij fits (the corresponding parameters are provided in Table VI).

of P-bearing molecules in the ISM.[117,118] This network already included the rates of the P + OH → PO + H and P + H_2O → PO + H_2 reactions[119] and that of P + O_2 → PO + O.[114] In this work, we have implemented the following changes:

1. First, we completely updated the gas-phase chemical network, replacing the old UMIST database (Rate12—McElroy *et al.*[120]) with the newer Rate22 version, presented in Ref. 78. We carefully compared both versions to track the changes regarding the P network. The new version contains 274 reactions involving P-bearing species. For four of them, the reaction parameters have been updated; 31 reactions are new additions that were not included in the previous version.
2. We cross-correlated our previous gas-phase P network and UMIST22, and we avoided duplication of the 14 reactions that were present in both networks with the same rates. For the reactions from Ref. 119 previously mentioned, we used the rates calculated in that work and not those present in UMIST22, which refer to the early guess[115] based on the N + OH → NO + H reaction as a reference.
3. Since PNH^+ is the low energy isomer, and we have shown that is the main product of the PN + H_3^+, PH + NH^+, and PH^++ NH reactions, we replaced HPN^+ in Rate22 by PNH^+. Similarly, we changed HPN to PNH, which is the lowest energy isomer.[121]
4. For the protonation reactions PN + H_3O^+ → H_2O + PNH^+ and PN + HCO^+ → CO + PNH^+, we used the reaction rates from the KIDA database,[77] based on the work of Woon and Herbst,[103] instead of those of UMIST22. This choice was motivated by two main reasons: (i) the KIDA values are consistent with the rates we calculated for the protonation of PN by $H_3{}^+$, as shown in Sec. III C 1, and (ii) the UMIST22 database assigns identical rate coefficients to all protonation reactions of PN, regardless of the proton donor, which may oversimplify the chemistry. Since the KIDA rates are not initially provided in Arrhenius–Kooij form (which is necessary for UCLCHEM), we fitted them as a function of temperature using the same procedure described in Sec. III C, thus obtaining the following values for the reactions with HCO^+(H_3O^+): $\alpha = 3.253 \times 10^{-9}$ (3.738×10^{-9}) cm^3 $molecule^{-1}$ s^{-1}, $\beta = -0.394$ (-0.394), and $\gamma = -1.778$ (-1.778) K.
5. We implemented the P + O_2 reaction studied in Ref. 114 and replaced the repeated entry in UMIST22.
6. We implemented the reaction rates derived in this work for the PH + NH^+ and PH^+ + NH reactions. We used the total reaction rates we have derived (see Sec. III C).

We have used a physical model that mimics the conditions of the Galactic Center molecular cloud G+0.693-0.027 (hereafter shortly denoted as G+0.693), where PN, PO, and the cation PO^+ have previously been detected. The chemistry of this source is characterized by low-velocity shocks (which explain the linewidths of the molecular emission of 15–20 km s^{-1}) and by an enhanced cosmic-ray ionization rate with respect to its standard value ($\zeta_0 \sim 10^{-14}$–10^{-15} s^{-1}).[14,122] UCLCHEM was run in three phases: (i) phase 0 considers the chemistry of a translucent cloud with n(H) $= 10^3$ cm^{-3} and $T_{\rm kin} = 20$ K for 10^6 yrs; (ii) phase 1 simulates the collapse of a molecular cloud from n(H) $= 10^3$ cm^{-3} to n(H) $= 2 \times 10^4$ cm^{-3} at a constant temperature of $T_{\rm kin} = 10$ K; and (iii) phase 2 simulates the passage of a low-velocity C-type shock with $v_s = 20$ km s^{-1} and initial gas density of n(H) $= 10^4$ cm^{-3} using the parametric approximation for the physical structure of the C-type shocks presented in Ref. 123. The assumed shock velocity of $v_s = 20$ km $^{-1}$ is consistent with the observed linewidths of the molecular line emission[124–126] and with the gas densities measured toward G+0.693.[127,128] To check the effect on the chemistry of the cosmic-ray ionization rate (ζ), we considered three cases with values 1, 100, and 1000 times the standard value $\zeta_0 = 1.3 \times 10^{-17}$ s^{-1}.

According to the chemical model, the dominant pathways for the formation of PNH^+ are those involving PN with HCO^+, H_3O^+,

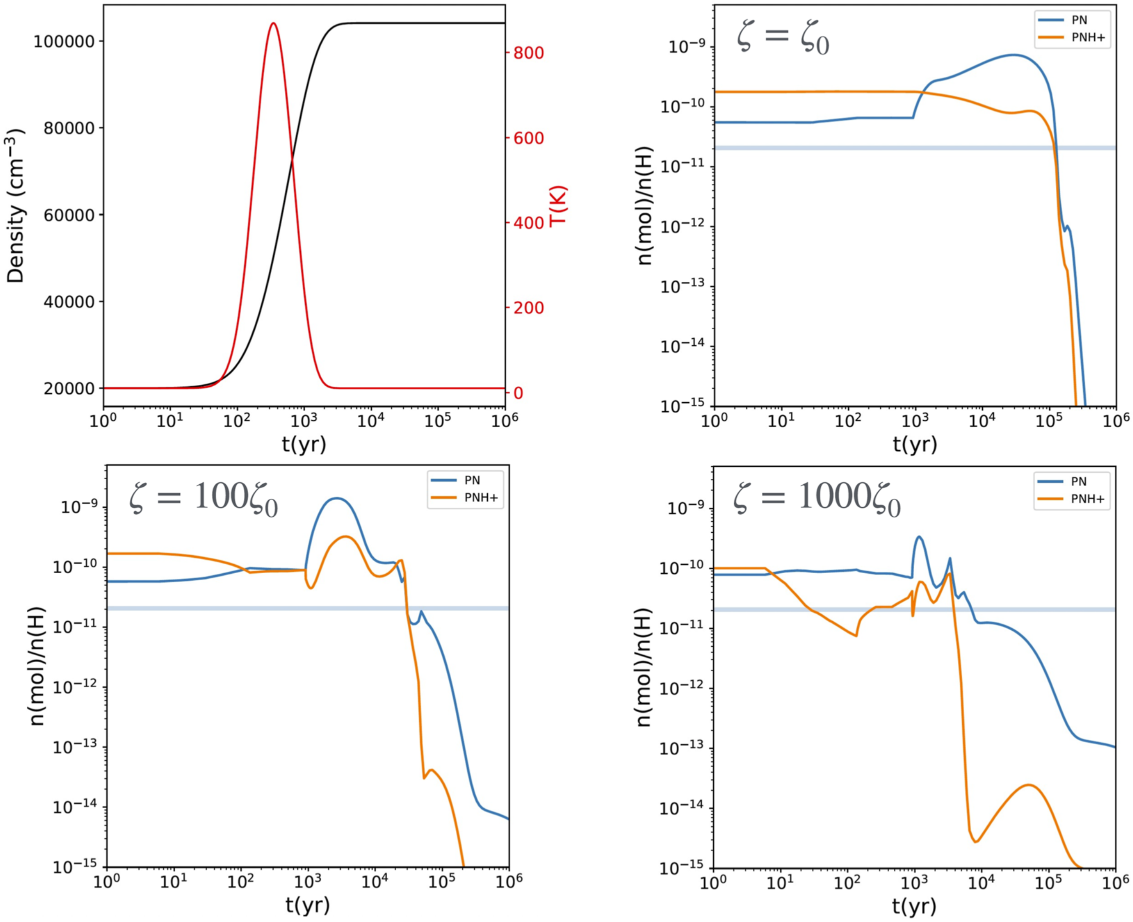

FIG. 8. Results of the astrochemical model for phase 2 (passage of a low-velocity shock), which mimics the physical environment of the G+0.693-0.027 molecular cloud. Upper left panel: evolution of the density (black curve) and temperature (red curve) during the shock phase. Upper right panel and lower panels: evolution of the abundances with respect to H, assuming $n(\mathrm{H}) = 2 \times n(\mathrm{H_2})$, of PN (blue) and PNH$^+$ (orange), as a function of time across a C-type shock with a preshock density of $n(\mathrm{H}) = 2 \times 10^4$ cm^{-3} and a shock speed of $v_s = 20$ km s^{-1}. Cosmic-ray ionization rates of 1, 100, and 1000 times of the standard value $\zeta_0 = 1.3 \times 10^{-15}$ s^{-1} are considered during the shock phase model. The blue band indicates the PN abundance with respect to H derived in Ref. 14.

and H_3^+, while the reactions involving PH and PH$^+$ explored in this work provide alternative formation routes that, although less competitive under the modeled conditions, expand the possible chemistry leading to PNH$^+$. Regarding the destruction of PNH$^+$, it is due to the electron recombination with a rate of ~2 × 10^{-12} cm^3 molecule^{-1} s^{-1}.

We show in Fig. 8 the results of phase 2 for PNH$^+$ and PN. The relative molecular ratio between both species is very sensitive to both the time-scales of the shock and the cosmic-ray ionization rate (ζ). We focus here in the range $100\zeta_0$–$1000\zeta_0$, which is the one inferred using other cations detected toward G+0.693.[14,122] At the time in which the PN abundance observed toward G+0.693 is reproduced, PNH$^+$ is similarly abundant than PN within a factor of 2 for $\zeta = 100\zeta_0$, while it is several orders of magnitude lower for $1000\zeta_0$, due to more efficient and faster destruction. Assuming the former case, the interstellar detectability of PNH$^+$ might be possible using the spectroscopic constants reported in this work, provided that astronomical line surveys cover several rotational transitions with sufficient sensitivity.

IV. CONCLUSIONS

We have reported a comprehensive spectroscopic characterization of the lowest-energy structure of protonated phosphorus mononitride, PNH$^+$($^1\Sigma^+$), using a state-of-the-art composite scheme entirely based on coupled-cluster theory and accounting for extrapolation to the complete basis set limit and higher excitations in the cluster expansion up to quadruples. All the spectroscopic parameters relevant to rotational, vibrational, and rovibrational spectroscopy have been evaluated with great accuracy in order to support future laboratory experiments and, possibly, to guide astronomical observations. In order to assess the uncertainties affecting our predictions, a benchmark study has also been carried out, which involved the isovalent N_2H^+, HCO^+, and HCS^+ cations, very well experimentally characterized.

Furthermore, we explored three astrochemically relevant reactions that can lead to the formation of PNH^+, including the protonation of neutral PN by H_3^+, as well as ion–neutral reactions not involving PN. The results indicate that $PNH^+(^1\Sigma^+)$ is likely to be the dominant isomer under interstellar conditions, although the formation of $HPN^+(^1\Sigma^+)$ is also expected, even to a lesser extent, particularly from the PH + NH^+ pathway. These findings emphasize that the formation of protonated phosphorus mononitride in the ISM should not be considered solely due to the protonation of existing PN. Instead, alternative formation pathways involving small radicals and cations may play a significant role. The astrochemical model developed here yields a predicted abundance of PNH^+ that can be comparable to that of PN. Consequently, detecting PNH^+ in the ISM might provide crucial insights. However, it is a significant challenge both observationally, in determining its actual abundance and its ratio with PN, and from a modeling perspective, should future detections reveal levels that deviate from current predictions.

The spectroscopic and kinetic results obtained in the framework of this work provide both an important input for astrochemical modeling and a theoretical framework to guide laboratory spectroscopy and thus astronomical searches for PNH^+. The identification of multiple viable formation pathways also reinforces the expected chemical richness of P-bearing species in the interstellar medium and opens new ways for future studies on their astrochemical evolution.

SUPPLEMENTARY MATERIAL

Tables reporting the energetics of the potential energy surfaces (PESs) and temperature-dependent rate coefficients for the studied ion–molecule reactions are provided in the supplementary material.

ACKNOWLEDGMENTS

This work was supported by MUR (PRIN Grant Nos. 202082CE3T, P2022ZFNBL, and 20225228K5) and by the University of Bologna (RFO funds). M.M. thanks the European Union—Next Generation EU under the Italian National Recovery and Resilience Plan (PNRR M4C2, Investment 1.4—Call for tender n. 3138 dated 16/12/2021—CN00000013 National Center for HPC, Big Data and Quantum Computing (HPC)—CUP J33C22001170001). D.C. acknowledges the CINECA award under the ISCRA initiative, for the availability of high performance computing resources and support (Project ID: IsCb8_PROMAS). We warmly thank Y. Georgievskii, S. J. Klippenstein, and C. Cavallotti for their valuable assistance with the MESS software and for constructive discussions that contributed to the improvement in this work. D.C. also thanks T. E. Field-Theodore and J. A. Claus for insightful discussions. V.M.R. and I.J.-S. acknowledge support from Grant No. PID2022-136814NB-I00 by the Spanish Ministry of Science, Innovation and Universities/State Agency of Research MICIU/AEI/10.13039/501100011033 and by ERDF, UE. V.M.R. also acknowledges support from Grant No. RYC2020-029387-I funded by MICIU/AEI/10.13039/501100011033 and by "ESF, Investing in your future"; from the Consejo Superior de Investigaciones Científicas (CSIC) and the Centro de Astrobiología (CAB) through Project No. 20225AT015 (Proyectos intramurales especiales del CSIC); and from Grant No. CNS2023-144464 funded by MICIU/AEI/10.13039/501100011033 and by "European Union NextGenerationEU/PRTR." I.J.-S. acknowledges funding from the ERC CoG grant OPENS (Project No. 101125858) funded by the European Union. We warmly thank Gijs Vermariën for his help for running UCLCHEM.

AUTHOR DECLARATIONS

Conflict of Interest

The authors have no conflicts to disclose.

Author Contributions

D. Comte: Formal analysis (lead); Investigation (equal); Software (lead); Writing – original draft (lead); Writing – review & editing (equal). **M. Melosso**: Conceptualization (lead); Project administration (lead); Supervision (equal); Writing – review & editing (equal). **S. Alessandrini**: Supervision (equal); Writing – review & editing (equal). **L. Bizzocchi**: Writing – review & editing (equal). **V. M. Rivilla**: Investigation (equal); Writing – review & editing (equal). **I. Jiménez-Serra**: Writing – review & editing (equal). **C. Puzzarini**: Funding acquisition (lead); Methodology (lead); Supervision (equal); Writing – review & editing (equal).

DATA AVAILABILITY

The data that support the findings of this study are available from the corresponding author upon reasonable request.

REFERENCES

[1] M. Butusov and A. Jernelöv, "The role of phosphorus in the origin of life and in evolution," in *Phosphorus: An Element that Could Have Been Called Lucifer* (Springer, 2013), pp. 1–12.

[2] F. Fontani, Front. Astron. Space Sci. **11**, 1451127 (2024).

[3] B. E. Turner and J. Bally, Astrophys. J. **321**, L75 (1987).

[4] L. M. Ziurys, Astrophys. J. **321**, L81 (1987).

[5] V. M. Rivilla, I. Jiménez-Serra, S. Zeng, S. Martín, J. Martín-Pintado *et al.*, Mon. Not. R. Astron. Soc. Lett. **475**, L30 (2018).

[6] F. Fontani, V. M. Rivilla, F. F. S. V. D. Tak, C. Mininni, M. T. Beltrán, and P. Caselli, Mon. Not. R. Astron. Soc. **489**, 4530 (2019).

[7] D. Haasler, V. M. Rivilla, S. Martín, J. Holdship, S. Viti, N. Harada *et al.*, Astron. Astrophys. **659**, A158 (2022).

[8] E. D. Tenenbaum, N. J. Woolf, and L. M. Ziurys, Astrophys. J. **666**, L29 (2007).

[9] M. Guélin, J. Cernicharo, G. Paubert, and B. E. Turner, Astron. Astrophys. **230**, L9 (1990).

[10] M. Agúndez, J. Cernicharo, J. R. Pardo, M. Guélin, and T. G. Phillips, Astron. Astrophys. **485**, L33 (2008).

[11] E. D. Tenenbaum and L. M. Ziurys, Astrophys. J. **680**, L121 (2008).

[12] M. Agúndez, J. Cernicharo, and M. Guélin, Astrophys. J. **662**, L91 (2007).

[13] D. T. Halfen, D. J. Clouthier, and L. M. Ziurys, Astrophys. J. **677**, L101 (2008).

[14] V. M. Rívilla, J. G. de La Concepción, I. Jiménez-Serra, J. Martín-Pintado, L. Colzi *et al.*, Front. Astron. Space Sci. **9**, 829288 (2022).

[15] S. Scibelli, A. Megías, I. Jiménez-Serra, Y. Shirley, J. Bergner *et al.*, Astrophys. J. Lett. **985**, L25 (2025).

[16] L. A. Koelemay, M. A. Burton, A. P. Singh, P. M. Sheridan, J. J. Bernal, and L. M. Ziurys, Astrophys. J., Lett. **940**, L11 (2022).

[17] E. Herbst, Int. Rev. Phys. Chem. **36**, 287 (2017).
[18] T. Oka, Proc. Natl. Acad. Sci. U. S. A. **103**, 12235 (2006).
[19] C. S. Contreras, L. V. Prieto, M. Agúndez, J. Cernicharo, G. Quintana-Lacaci *et al.*, Astron. Astrophys. **577**, A52 (2015).
[20] W. M. Irvine, J. C. Good, and F. P. Schloerb, Astron. Astrophys. **127**, L10 (1983).
[21] D. Quénard, C. Vastel, C. Ceccarelli, P. Hily-Blant, B. Lefloch, and R. Bachiller, Mon. Not. R. Astron. Soc. **470**, 3194 (2017).
[22] A. Bacmann, E. García-García, and A. Faure, Astron. Astrophys. **588**, L8 (2016).
[23] D. Skouteris, N. Balucani, C. Ceccarelli, N. Faginas Lago, C. Codella, S. Falcinelli, and M. Rosi, Mon. Not. R. Astron. Soc. **482**, 3567 (2019).
[24] V. Richardson, D. B. Rap, S. Brünken, and D. Ascenzi, Mol. Phys. **122**, e2223079 (2024).
[25] D. Comte, L. Lavy, P. Bertier, F. Calvo, I. Daniel *et al.*, J. Phys. Chem. A **127**, 775 (2023).
[26] D. Comte, L. Lavy, L. Parrado-Ospina, H. Lissillour, P. Bertier, F. Calvo, I. Daniel, B. Farizon, and M. Farizon, Phys. Scr. **100**, 015415 (2025).
[27] C. Puzzarini, S. Alessandrini, L. Bizzocchi, M. Melosso, and V. M. Rivilla, Front. Astron. Space Sci. **10**, 1211784 (2023).
[28] G. Santra, N. Sylvetsky, and J. M. L. Martin, J. Phys. Chem. A **123**, 5129 (2019).
[29] S. Grimme, J. Antony, S. Ehrlich, and H. Krieg, J. Chem. Phys. **132**, 154104 (2010).
[30] S. Grimme, S. Ehrlich, and L. Goerigk, J. Comput. Chem. **32**, 1456 (2011).
[31] T. H. Dunning, Jr., J. Chem. Phys. **90**, 1007 (1989).
[32] E. Papajak and D. G. Truhlar, J. Chem. Theory Comput. **7**, 10 (2011).
[33] I. M. Mills, "Vibration-rotation structure in asymmetric- and symmetric-top molecules," in *Molecular Spectroscopy: Modern Research*, edited by K. N. Rao and C. W. Mathews (Academic Press, New York, 1972), pp. 115–140.
[34] C. Puzzarini, J. F. Stanton, and J. Gauss, Int. Rev. Phys. Chem. **29**, 273 (2010).
[35] N. Vogt, J. Vogt, and J. Demaison, J. Mol. Struct. **988**, 119 (2011).
[36] C. Puzzarini, M. Heckert, and J. Gauss, J. Chem. Phys. **128**, 194108 (2008).
[37] D. E. Woon and T. H. Dunning, Jr., J. Chem. Phys. **98**, 1358 (1993).
[38] A. K. Wilson, T. V. Mourik, and T. H. Dunning, Jr., J. Mol. Struct.: THEOCHEM **388**, 339 (1996).
[39] T. V. Mourik and T. H. Dunning, Jr., Int. J. Quantum Chem. **76**, 205 (2000).
[40] D. Feller, J. Chem. Phys. **96**, 6104 (1992).
[41] K. Raghavachari, G. W. Trucks, J. A. Pople, and M. Head-Gordon, Chem. Phys. Lett. **157**, 479 (1989).
[42] T. Helgaker, W. Klopper, H. Koch, and J. Noga, J. Chem. Phys. **106**, 9639 (1997).
[43] D. E. Woon and T. H. Dunning, Jr., J. Chem. Phys. **103**, 4572 (1995).
[44] K. A. Peterson and T. H. Dunning, Jr., J. Chem. Phys. **117**, 10548 (2002).
[45] G. E. Scuseria and H. F. Schaefer III, Chem. Phys. Lett. **152**, 382 (1988).
[46] J. D. Watts and R. J. Bartlett, J. Chem. Phys. **93**, 6104 (1990).
[47] S. A. Kucharski and R. J. Bartlett, J. Chem. Phys. **97**, 4282 (1992).
[48] M. Kállay and P. R. Surján, J. Chem. Phys. **115**, 2945 (2001).
[49] P. Pyykkö, Mol. Phys. **106**, 1965 (2008).
[50] M. Tokman, D. Sundholm, P. Pyykkö, and J. Olsen, Chem. Phys. Lett. **265**, 60 (1997).
[51] A. Rizzo, C. Puzzarini, S. Coriani, and J. Gauss, J. Chem. Phys. **124**, 064302 (2006).
[52] W. H. Flygare, Chem. Rev. **74**, 653 (1974).
[53] L. Bizzocchi, S. Alessandrini, M. Melosso, and C. Puzzarini, Phys. Chem. Chem. Phys. **24**, 15173 (2022).
[54] J. Gauss, K. Ruud, and T. Helgaker, J. Chem. Phys. **105**, 2804 (1996).
[55] J. Gauss and J. F. Stanton, J. Chem. Phys. **104**, 2574 (1996).
[56] J. F. Stanton, J. Gauss, L. Cheng, M. E. Harding, D. A. Matthews, P. G. Szalay *et al.*, CFOUR, a quantum chemical program package, for the current version, see http://www.cfour.de.
[57] D. A. Matthews, L. Cheng, M. E. Harding, F. Lipparini, S. Stopkowicz, T.-C. Jagau, P. G. Szalay, J. Gauss, and J. F. Stanton, J. Chem. Phys. **152**, 214108 (2020).
[58] M. J. Frisch, G. W. Trucks, H. B. Schlegel, G. E. Scuseria, M. A. Robb, J. R. Cheeseman *et al.*, Gaussian 16, Gaussian, Inc., Wallingford, CT, 2016.
[59] K. Fukui, Acc. Chem. Res. **14**, 363 (1981).
[60] H. Ye, S. Alessandrini, and C. Puzzarini, Astrophys. J. **962**, 32 (2024).
[61] S. Alessandrini, L. Bizzocchi, M. Melosso, and C. Puzzarini, Front. Astron. Space Sci. **10**, 1128896 (2023).
[62] S. Alessandrini, V. Barone, and C. Puzzarini, J. Chem. Theory Comput. **16**, 988 (2019).
[63] S. Alessandrini, F. Tonolo, and C. Puzzarini, J. Chem. Phys. **154**, 054306 (2021).
[64] H. Ye, S. Alessandrini, and C. Puzzarini, Mon. Not. R. Astron. Soc. **525**, 1158 (2023).
[65] Y. Georgievskii and S. J. Klippenstein, J. Chem. Phys. **122**, 194103 (2005).
[66] S. J. Klippenstein, Y. Georgievskii, and B. J. McCall, J. Phys. Chem. A **114**, 278 (2010).
[67] Y. Georgievskii and S. J. Klippenstein, MESS. 2016.3.23, Argonne National Laboratory, 2016.
[68] Y. Georgievskii, J. A. Miller, M. P. Burke, and S. J. Klippenstein, J. Phys. Chem. A **117**, 12146 (2013).
[69] C. Eckart, Phys. Rev. **35**, 1303 (1930).
[70] D. M. Kooij, ZPC **12**, 155 (1893).
[71] R. Glaser, C. J. Horan, and P. E. Haney, J. Phys. Chem. **97**, 1835 (1993).
[72] R. G. A. R. Maclagan, J. Phys. Chem. **94**, 3373 (1990).
[73] R. J. Buenker, P. J. Bruna, and S. D. Peyerimhoff, Isr. J. Chem. **19**, 309 (1980).
[74] Y.-N. Su, M.-S. Tsai, and S.-Y. Chu, Int. J. Quantum Chem. **59**, 487 (1996).
[75] A. Largo, J. R. Flores, C. Barrientos, and J. M. Ugalde, J. Phys. Chem. **95**, 170 (1991).
[76] N. G. Adams, B. J. McIntosh, and D. Smith, Astron. Astrophys. **232**, 443 (1990).
[77] V. Wakelam, E. Herbst, J.-C. Loison, I. W. M. Smith, V. Chandrasekaran, B. Pavone, N. G. Adams, M.-C. Bacchus-Montabonel, A. Bergeat, K. Béroff *et al.*, Astrophys. J., Suppl. Ser. **199**, 21 (2012).
[78] T. J. Millar, C. Walsh, M. V. de Sande, and A. J. Markwick, Astron. Astrophys. **682**, A109 (2024).
[79] N. Harada, S. Martín, J. G. Mangum, K. Sakamoto, S. Muller *et al.*, Astrophys. J. **923**, 24 (2021).
[80] C. Puzzarini and J. F. Stanton, Phys. Chem. Chem. Phys. **25**, 1421 (2023).
[81] M. Mladenović, J. Chem. Phys. **147**, 114111 (2017).
[82] M. Mladenović and M. Lewerenz, J. Mol. Spectrosc. **383**, 111567 (2022).
[83] L. Margulès, F. Lewen, G. Winnewisser, P. Botschwina, and H. S. P. Müller, Phys. Chem. Chem. Phys. **5**, 2770 (2003).
[84] G. Cazzoli, L. Cludi, G. Buffa, and C. Puzzarini, Astrophys. J., Suppl. Ser. **203**, 11 (2012).
[85] X. Huang, E. F. Valeev, and T. J. Lee, J. Chem. Phys. **133**, 244108 (2010).
[86] J. Koput, J. Chem. Phys. **150**, 154307 (2019).
[87] C. Puzzarini, J. Chem. Phys. **123**, 024313 (2005).
[88] B. Schröder and P. Sebald, J. Mol. Spectrosc. **330**, 120 (2016).
[89] M. Havenith, E. Zwart, W. L. Meerts, and J. J. T. Meulen, J. Chem. Phys. **93**, 8446 (1990).
[90] P. Botschwina, Chem. Phys. Lett. **107**, 535 (1984).
[91] P. Botschwina, M. Horn, J. Flügge, and S. Seeger, J. Chem. Soc., Faraday Trans. **89**, 2219 (1993).
[92] P. Botschwina and P. Sebald, J. Mol. Spectrosc. **110**, 1 (1985).
[93] P. Caselli, P. C. Myers, and P. Thaddeus, Astrophys. J. **455**, L77 (1995).
[94] T. J. Sears, J. Opt. Soc. Am. B **2**, 786 (1985).
[95] S. C. Foster and A. R. W. McKellar, J. Chem. Phys. **81**, 3424 (1984).
[96] T. Nakanaga, F. Ito, K. Sugawara, H. Takeo, and C. Matsumura, Chem. Phys. Lett. **169**, 269 (1990).
[97] K. Kawaguchi, C. Yamada, S. Saito, and E. Hirota, J. Chem. Phys. **82**, 1750 (1985).
[98] S. C. Foster, A. R. W. McKellar, and T. J. Sears, J. Chem. Phys. **81**, 578 (1984).
[99] T. Amano, J. Chem. Phys. **79**, 3595 (1983).
[100] N. H. Rosenbaum, J. C. Owrutsky, L. M. Tack, and R. J. Saykally, J. Chem. Phys. **83**, 4845 (1985).
[101] P. B. Davies and W. J. Rothwell, J. Chem. Phys. **83**, 1496 (1985).
[102] V. Wakelam, I. W. M. Smith, E. Herbst, J. Troe, W. Geppert *et al.*, Space Sci. Rev. **156**, 13 (2010).
[103] D. E. Woon and E. Herbst, Astrophys. J., Suppl. Ser. **185**, 273 (2009).
[104] D. D. S. MacKay and S. B. Charnley, Mon. Not. R. Astron. Soc. **325**, 545 (2001).

[105] D. M. Meyer and K. C. Roth, Astrophys. J. **376**, L49 (1991).
[106] Z. Qin, J. M. Zhao, and L. H. Liu, J. Quant. Spectrosc. Radiat. Transfer **227**, 47 (2019).
[107] J. Hoeft, E. Tiemann, and T. Törring, Z. Naturforsch. A **27**, 703 (1972).
[108] J. Raymonda and W. Klemperer, J. Chem. Phys. **55**, 232 (1971).
[109] H. S. P. Müller, S. Thorwirth, D. A. Roth, and G. Winnewisser, Astron. Astrophys. **370**, L49 (2001).
[110] H. S. P. Müller and D. E. Woon, J. Phys. Chem. A **117**, 13868 (2013).
[111] T. A. R. Irwin and F. W. Dalby, Can. J. Phys. **43**, 1766 (1965).
[112] C. E. Dateo and D. C. Clary, J. Chem. Phys. **90**, 7216 (1989).
[113] J. Holdship, S. Viti, I. Jiménez-Serra, A. Makrymallis, and F. Priestley, Astron. J. **154**, 38 (2017).
[114] J. G. de la Concepción, C. Cavallotti, V. Barone, C. Puzzarini, and I. Jiménez-Serra, Astrophys. J. **963**, 142 (2024).
[115] I. Jiménez-Serra, S. Viti, D. Quénard, and J. Holdship, Astrophys. J. **862**, 128 (2018).
[116] M. Asplund, N. Grevesse, A. J. Sauval, and P. Scott, Annu. Rev. Astron. Astrophys. **47**, 481 (2009).
[117] T. Aota and Y. Aikawa, Astrophys. J. **761**, 74 (2012).
[118] B. Lefloch, C. Vastel, S. Viti, I. Jiménez-Serra, C. Codella *et al.*, Mon. Not. R. Astron. Soc. **462**, 3937 (2016).
[119] J. G. de la Concepción, C. Puzzarini, V. Barone, I. Jiménez-Serra, and O. Roncero, Astrophys. J. **922**, 169 (2021).
[120] D. McElroy, C. Walsh, A. J. Markwick, M. A. Cordiner, K. Smith, and T. J. Millar, Astron. Astrophys. **550**, A36 (2013).
[121] R. B. Viana, P. S. S. Pereira, L. G. M. Macedo, and A. S. Pimentel, Chem. Phys. **363**, 49 (2009).
[122] M. Sanz-Novo, V. M. Rivilla, I. Jiménez-Serra, J. Martín-Pintado, L. Colzi *et al.*, Astrophys. J. **965**, 149 (2024).
[123] I. Jiménez-Serra, P. Caselli, J. Martín-Pintado, and T. W. Hartquist, Astron. Astrophys. **482**, 549 (2008).
[124] M. A. Requena-Torres, J. Martín-Pintado, A. Rodríguez-Franco, S. Martín, N. J. Rodríguez-Fernández, and P. de Vicente, Astron. Astrophys. **455**, 971 (2006).
[125] S. Zeng, I. Jiménez-Serra, V. M. Rivilla, S. Martín, J. Martín-Pintado, M. A. Requena-Torres *et al.*, Mon. Not. R. Astron. Soc. **478**, 2962 (2018).
[126] V. M. Rivilla, I. Jiménez-Serra, J. Martín-Pintado, L. Colzi, B. Tercero, P. de Vicente *et al.*, Front. Astron. Space Sci. **9**, 876870 (2022).
[127] S. Zeng, Q. Zhang, I. Jiménez-Serra, B. Tercero, X. Lu, J. Martín Pintado *et al.*, Mon. Not. R. Astron. Soc. **497**, 4896 (2020).
[128] L. Colzi, J. Martín-Pintado, S. Zeng, I. Jiménez-Serra, V. M. Rivilla, M. Sanz-Novo *et al.*, Astron. Astrophys. **690**, A121 (2024).